Self-assembly of semiconductor nanocrystals into ordered superstructures

By

Elena V. Shevchenko[1], **Dmitri V. Talapin**[2]

[1] Center for Nanoscale Materials, Argonne National Lab, Argonne, IL, USA
[2] Department of Chemistry, University of Chicago, Chicago, IL, USA

1. Introduction

Organization of uniform objects into periodic structures can be found in many natural systems, such as atomic and molecular solids, opals, sponges and bacterial colonies – self-assembly is the fundamental phenomenon that generates structural organization on all scales [1]. In this chapter we discuss the structures spontaneously formed by nanoparticles which attracted significant interest from different branches of science and technology. The progress in colloidal synthesis of inorganic nanomaterials enabled preparation of different materials (metals, semiconductors, magnetic and ferroelectric materials) in the form of uniform nanometer-size crystals with amazing levels of size and shape control [2]. Nowadays colloidal synthesis allows for creation of nanostructures where composition, size, shape and connectivity of multiple parts of a multicomponent structure can be tailored in an independent and predictable manner (Fig. 1). In many nanoscale materials size and shape control provides additional degrees of freedom for designing physical and chemical properties. Thus, the effect of quantum confinement allows fine-tuning of the optical and electronic properties of semiconductor nanoparticles through varying particle size [3]. Exchange-biased ferromagnetism [4], size-dependent magnetic and catalytic properties of sub-20 nm particles are all examples of how material properties can be tailored by size and shape engineering at the nanoscale [5, 6].

Unique size tunable physical and electronic properties of the individual nanoparticles have prompted some researchers to refer to them as “artificial atoms”. As the number of nanoparticle systems under strict synthetic control has expanded, the parallels to the development of a “new periodic table” have been discussed. Following this analogy, the ability to assemble “artificial atoms” into ordered one-, two- and three-dimensional structures (superlattices) should lead to creation of novel class of “artificial solids” with tunable properties determined both by the properties of individual nanoparticle constituents and the collective physical properties of the superlattice. In contrast to random mixtures of nanoparticles, the ordered nanoparticle arrays provide precise uniformity of packing and rigorous control of the

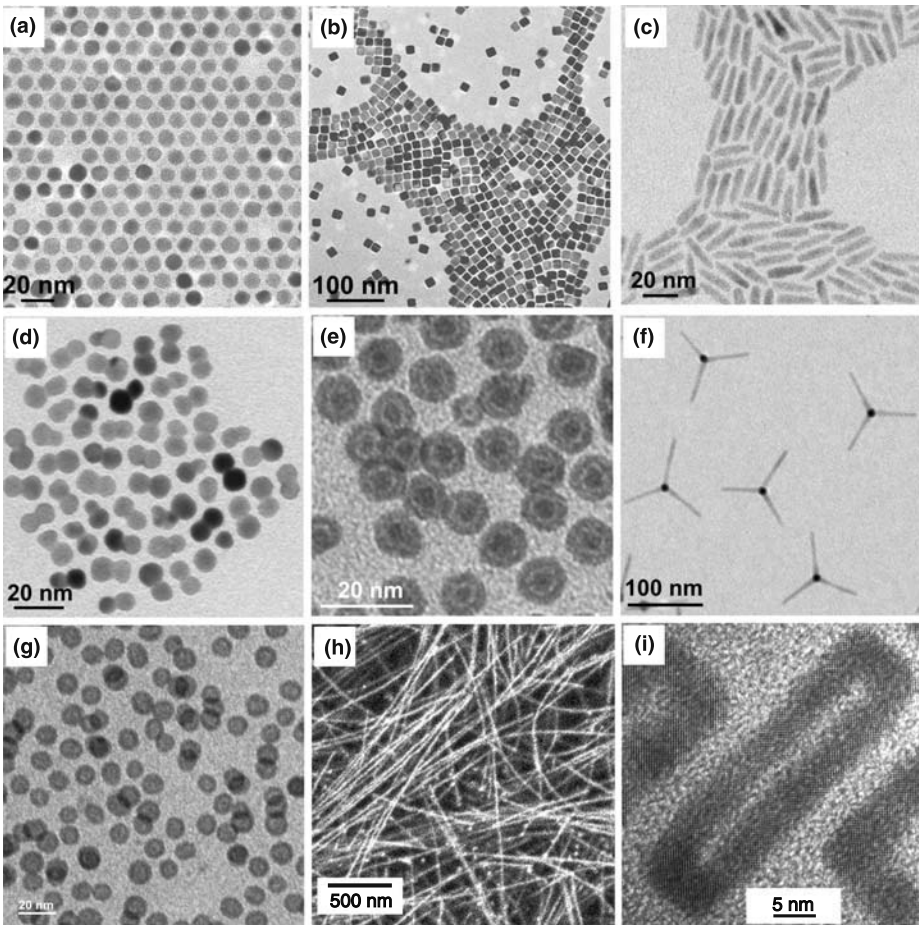

Fig. 1. Examples of semiconductor and magnetic nanomaterials of different sizes, shapes and compositions synthesized by colloidal chemistry techniques: **a** nearly spherical PbS nanocrystals; **b** PbSe nanocubes; **c** heterostructured CdSe/CdS nanorods; **d** $CoPt_3$/Au nanodumbbells; **e** nested iron–iron oxide nanostructures; **f** CdSe/CdS nanotetrapods; **g** hollow iron oxide nanoparticles; **h** PbSe nanowires; **i** PbSe nanorings

interparticle distances. Such structures, too small to be produced by existing lithographic "top down" approaches, can be generated by self-assembly which takes advantage of natural forces and organizes different pieces into desired architectures. In other words, novel materials or devices can be built by themselves and scientists merely have to find means to direct the self-assembly process [1].

2. Self-assembly of monodisperse quasi-spherical nanoparticles

Among the variety of objects that can self-assemble into ordered structures, uniform spheres are the simplest model system. Ordering of spherical particles has

been extensively studied both theoretically and experimentally [7–9]. In the case of nano- and microparticles, the most popular approach to form ordered superstructures is the dispersing particles in an appropriate carrier solvent followed by gradual increase of particle concentration by solvent evaporation. Depending on nanoparticle concentration, solvent, temperature, substrate, etc., different types of nanoparticle aggregates can be obtained. These can be characterized using optical, transmission electron (TEM) and scanning electron (SEM) microscopies, small-angle X-ray scattering (SAXS), X-ray diffraction (XRD) and electron diffraction (ED) techniques. Optical microscopy allows characterization of the shape of nanoparticle superlattices only, whereas electron microscopy and X-ray diffraction allow for insight into details of the local structure of nanoparticle assemblies. Both TEM and SEM provide real-space two-dimensional projections of superlattice structure. TEM generally has significantly higher resolution than SEM, however, it can be applied only to thin (typically sub-100 nm) samples transparent to the electron beam. The details of three-dimensional arrangements of particles can be reconstructed from a series of TEM images taken by tilting the sample by different angles. We would like to point the reader to the excellent review by Wang on TEM characterization of nanoparticle assemblies [10]. SAXS, small-angle XRD and ED techniques are frequently used to obtain quantitative information about symmetry and lattice parameters of nanoparticle assemblies [11].

2.1 Particle interactions. The assembly of nanoscale building blocks into macroscopic structures is driven by the interactions of particles with other particles, substrate, solvent, etc. Sometimes the driving force can be rather counterintuitive. Thus, *entropy* can drive *ordering* of hard spheres in three dimensions because of the increased local free space available for each sphere (i.e., its translational entropy) in the ordered lattice compared to the disordered state [7]. The entropy driven crystallization well describes self-assembly of micron-size polymer beads which can be modeled by non-interacting hard spheres. At the same time, metal and semiconductor nanoparticles usually exhibit strong interparticle electrostatic interactions [12, 13]. In addition to static electric charge, nanocrystals can exhibit large dipole moments and polarizabilities [14–16]; large Hamaker constants result in strong van der Waals attraction [17]. The pair potential for two charged nanocrystals should take into account multiple interactions including sterical and osmotic repulsion, van der Waals attraction, and electrostatic terms for zeroth and higher order moments of charge distribution (charge–charge, charge–dipole, dipole–dipole, charge–induced dipole, etc.):

$$V = V_{\text{steric}} + V_{\text{osmotic}} + V_{\text{vdW}} + V_{\text{Coulomb}} + V_{\text{charge-dipole}} + V_{\text{dipole-dipole}} + V_{\text{charge-ind.dipole}} \quad (1)$$

The Coulomb potential between two nanoparticles with charges Z_A and Z_B is

$$V_{\text{Coulomb}} \approx \frac{Z_A Z_B e^2}{4\pi\varepsilon\varepsilon_0 R} \quad (2)$$

where R is the center-to-center interparticle distance and ε is the static dielectric constant of the surrounding medium.

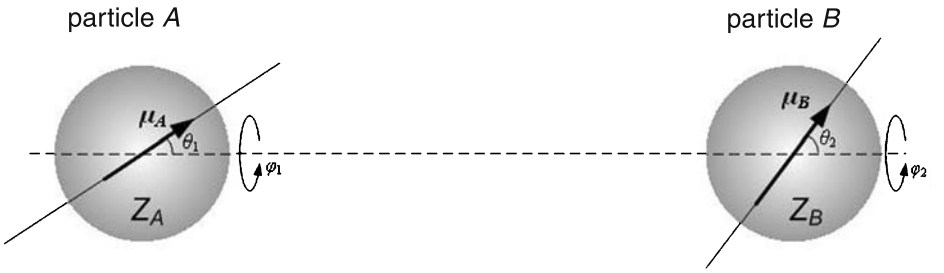

Fig. 2. Charge–dipole and dipole–dipole nanoparticle interactions. Interaction energy depends on the orientation of nanoparticle dipoles described by angles θ_1, θ_2, φ_1 and φ_2 in Eqs. (3) and (4)

The potential energy for charge–dipole, dipole–dipole and charge–induced dipole interactions between the particles A and B can be calculated as follows:

$$\text{charge}-\text{dipole}: V_{\text{charge}-\text{dipole}} = -\frac{e}{4\pi\varepsilon\varepsilon_0 R^2}\left(Z_{\text{A}}\mu_{\text{B}}\cos\theta_1 - Z_{\text{B}}\mu_{\text{A}}\cos\theta_2\right) \quad (3)$$

$$\text{dipole}-\text{dipole}: V_{\text{dipole}-\text{dipole}} = -\frac{\mu_{\text{A}}\mu_{\text{B}}(2\cos\theta_2\cos\theta_2 - \sin\theta_1\sin\theta_2\cos(\phi_2-\phi_1))}{4\pi\varepsilon\varepsilon_0 R^3} \quad (4)$$

$$\text{charge}-\text{induced dipole}: V_{\text{charge}-\text{ind.dipole}} = -\frac{e^2}{32\pi^2\varepsilon^2\varepsilon_0^2 R^4}\left(\alpha_{\text{A}}Z_{\text{B}}^2 + \alpha_{\text{B}}Z_{\text{A}}^2\right) \quad (5)$$

where μ_{A} and μ_{B} are dipole moments of particles A and B, respectively; θ_1, θ_2, φ_1 and φ_2 are the angles describing dipole orientations (Fig. 2); α_{A} and α_{B} are polarizabilities of particles A and B, respectively.

Dispersive (van der Waals) potential between two nanoparticles of radii R_{A} and R_{B} at the distance of closest approach D is

$$V_{\text{vdW}} = -\frac{A}{12}\left\{\frac{S}{D[1+D/2(R_{\text{A}}+R_{\text{B}})]} + \frac{1}{1+D/S+D^2/4R_{\text{A}}R_{\text{B}}} + 2\ln\left(\frac{D[1+D/2(R_{\text{A}}+R_{\text{B}})]}{R[1+D/S+D^2/4R_{\text{A}}R_{\text{B}}]}\right)\right\} \quad (6)$$

where A is the solvent-retarded Hamaker constant and $S = 2R_{\text{A}}R_{\text{B}}/(R_{\text{A}}+R_{\text{B}})$ is the reduced radius.

The short-range repulsion can be estimated as follows [18]:

$$V_{\text{repulsion}} \approx \frac{100S\delta^2}{(R-2S)\pi\sigma^2} kT\exp\left(-\frac{\pi(R-2S)}{\delta}\right) \quad (7)$$

where δ is the apparent thickness of the ligand shell around nanoparticle core, and σ is the diameter of the area occupied by the ligand anchor group on the particle

Table 1. Magnitudes of interactions between two 3 nm/5 nm semiconductor or metal nanoparticles with charges $Z = \pm e$ and dipoles oriented along the particle–particle axis

Interaction	$V_{\text{semiconductor–semiconductor}}$ (eV)		$V_{\text{metal–metal}}$ (eV)	
	$R = 6$ nm	$R = 10$ nm	$R = 6$ nm	$R = 10$ nm
Coulomb ($\sim 1/R$)	0.12	0.072	0.12	0.072
charge–dipole ($\sim 1/R^2$)	0.082	0.029	–	–
dipole–dipole ($\sim 1/R^3$)	0.028	5.8×10^{-3}	–	–
charge–induced dipole ($\sim 1/R^4$)	8.4×10^{-3}	1.1×10^{-3}	0.018	2.3×10^{-3}
van der Waals ($\sim 1/R^6$)	0.016	2.1×10^{-4}	0.097	1.3×10^{-3}

R is the particle center-to-center distance

surface. More precise descriptions for the short-range nanoparticle repulsion can be found in [19, 20].

Substitution of the expressions (2)–(6) into (1) allows estimation of the interparticle potentials for typical dielectric (semiconducting) and metallic nanoparticles. Table 1 provides estimated magnitudes of the interactions between two 3 nm/5 nm semiconductor nanocrystals with charge $Z = \pm e$, dipole moments $\mu = 100$ D and polarizabilities $\alpha/4\pi\varepsilon_0 = 30\ \text{nm}^3$ (these values are typical for CdSe nanocrystals [14, 15]) and two 3 nm/5 nm metal (e.g., Au) nanoparticles with charge $Z = \pm e$ and polarizabilities $\alpha/4\pi\varepsilon_0 = 65\ \text{nm}^3$ ($\sim$ nanoparticle volume). One can see that for semiconductors the energy of charge–dipole, dipole–dipole and charge–induced dipole interactions can approach $\sim 68\%$, 23% and 7% of Coulomb energy, respectively, when the particle separation is ~ 1 nm (the typical thickness of interdigitated capping ligands). Depending on the orientation of the nanoparticle dipole moments,

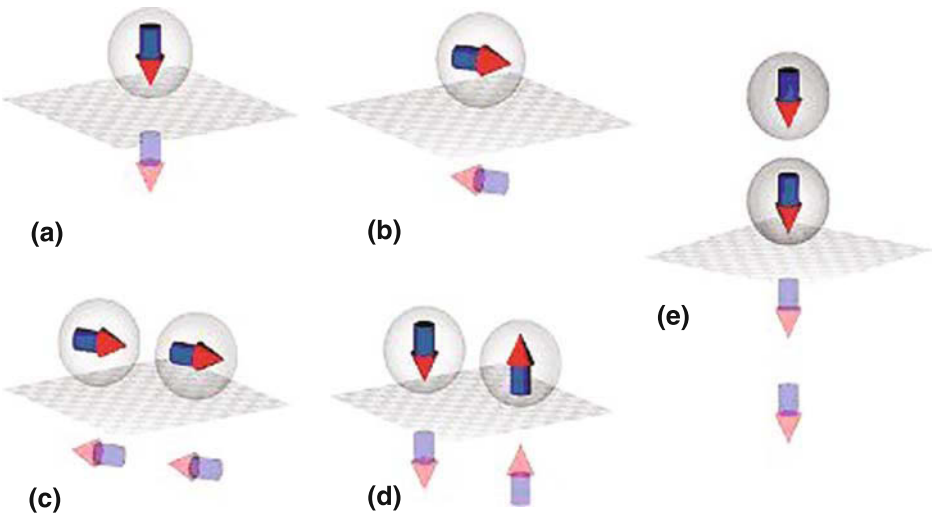

Fig. 3. Interaction of charged and dipolar nanoparticles with substrate can occur through the image charges. Reproduced from [23], © 2007, with permission from American Chemical Society

these additional terms can double (or cancel) electrostatic interactions between adjacent nanoparticles. This situation is quite unique. For example, for charged small molecules the Coulomb interactions dominate over dipolar and dispersive interactions by orders of magnitude [21].

When charged or dipolar nanoparticles are in close proximity with a conducting wall (e.g., a conducting carbon substrate), free electrons in the substrate screen the electric field of the charges and dipoles [22], which leads to an additional energy term due to the Coulombic coupling of all charges and dipoles with their mirror images (Fig. 3) [23].

In addition to electrostatic interactions, the hard inorganic core of a nanoparticle is surrounded with a "soft" layer of surfactant molecules. It was shown that surfactants can influence the assembly of NPs [24]. Thus, $Au_{140}(C_{12}H_{25}S)_{62}$ clusters capped with long-chain thiols are predicted to pack into 3D tetragonal superlattice whereas $Au_{140}(C_4H_9S)_{62}$ should form bcc superlattice [24]. Hydrophobic interactions between the ligands at the surface of CdTe nanocrystals stabilized with 2-(dimethylamino)ethanethiol can lead to spontaneous formation of 2D, free-floating sheets consisting of individual CdTe nanoparticles, as will be discussed in Sect. 2.3 [25].

The intrinsic complexity of the nanoparticle interactions introduces significant flexibility and the ability to manipulate the thermodynamics of their self-assembly by external parameters such as solvent, surfactants, temperature, external electric and magnetic fields. Proper tailoring of experimental conditions can lead to the formation of various amazing structures discussed in the following sections of this chapter.

2.2 Self-assembly of nanoparticles into one-dimensional structures. Semiconductor nanocrystals with large dipole moments can form chains in a colloidal solution due to strong dipole–dipole interactions. Nanoparticle chaining in solution has been recently documented by direct cryo-TEM studies of colloidal solutions of PbSe nanocrystals [26]. In the chains, the nanoparticles can fuse together by the mechanism of oriented attachment along identical crystal faces forming single-crystalline nanowires [27, 28]. The formation of nanowires via self-assembly of nanoparticles has been studied for several materials [27–29]. Weller and coworkers reported the formation of ZnO nanorods by oriented attachment of ZnO nanoparticles along the unique axis of its wurtzite crystal lattice [28]. The suggested aggregation mechanism is based on the difference in surface structure and reactivity of the (0 0 2) and (0 0 $\bar{2}$) faces of the wurtzite lattice. Tang et al. demonstrated that wurtzite, CdTe nanowires can be formed from zinc blend, CdTe nanocrystals after partial removal of the stabilizing agents from the nanocrystals' surfaces [27]. The cubic, zinc blend, CdTe nanocrystals formed chain like aggregates due to dipole–dipole interactions at the early stage of wire formation and then slowly re-crystallized into hexagonal, wurtzite, CdTe nanowires.

The inherent anisotropy of crystal structure or crystal surface reactivity was identified in previous studies as the driving force for the one-dimensional growth. In nanoparticles with wurtzite structure (e.g., CdSe), an electric dipole moment originates from the noncentrosymmetric atomic lattice and scales with the nanoparticle volume [14, 30]. However, in some nanoparticle systems the chaining of

nanoparticles into one-dimensional structure may look very counterintuitive. For example, PbSe nanocrystals have rocksalt type highly symmetric cubic crystal lattice. To form a 10-μm long nanowire, more than 10^3 individual nanocrystals must assemble and attach along one ⟨1 0 0⟩ axis while each PbSe nanocrystal has six equivalent ⟨1 0 0⟩ facets. Here, the dipolar interactions should be the driving force directing PbSe nanocrystals to assemble into chains. The origin of the dipoles in nanoparticles with centrosymmetric atomic unit cell could be explained by asymmetric lattice truncations [14] or noncentrosymmetric arrangement of Pb- and Se-terminated {1 1 1} facets [29]. Indeed, the reconstruction of the high-resolution TEM images revealed that PbSe nanocrystals are terminated by six {1 0 0} and eight {1 1 1} facets. The {1 0 0} facets are formed by both Pb and Se atoms while the {1 1 1} facets must be either Se- or Pb-terminated (Fig. 4a–c). Due to the difference in electronegativities between Pb and Se, {1 1 1} facets are polar and their arrangement will determine the distribution of electric charge within the PbSe nanocrystal.

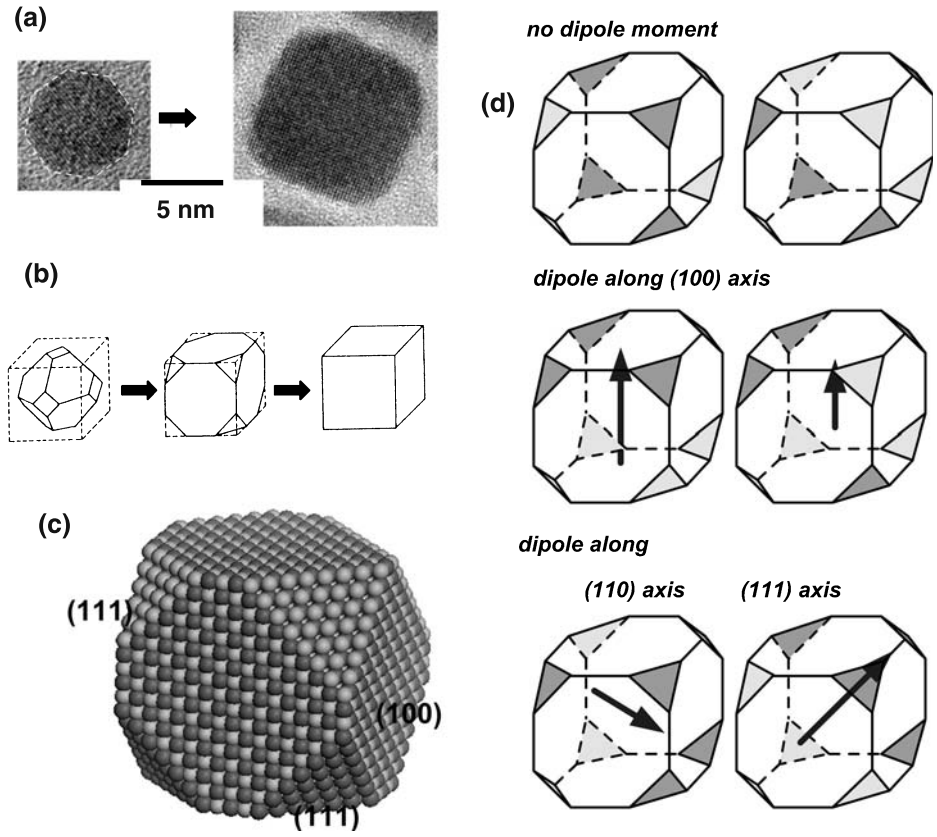

Fig. 4. **a** HRTEM images showing the typical evolution of the PbSe nanocrystal shape upon growth, as schematically depicted in **b**. **c** Atomic reconstruction of a rocksalt PbSe nanocrystal showing the structural difference between the ⟨1 0 0⟩ and ⟨1 1 1⟩ facets. **d** Different arrangements of polar ⟨1 1 1⟩ facets result in various orientations and magnitudes of the nanocrystal dipole moment. Reproduced from [29], © 2005, with permission from American Chemical Society

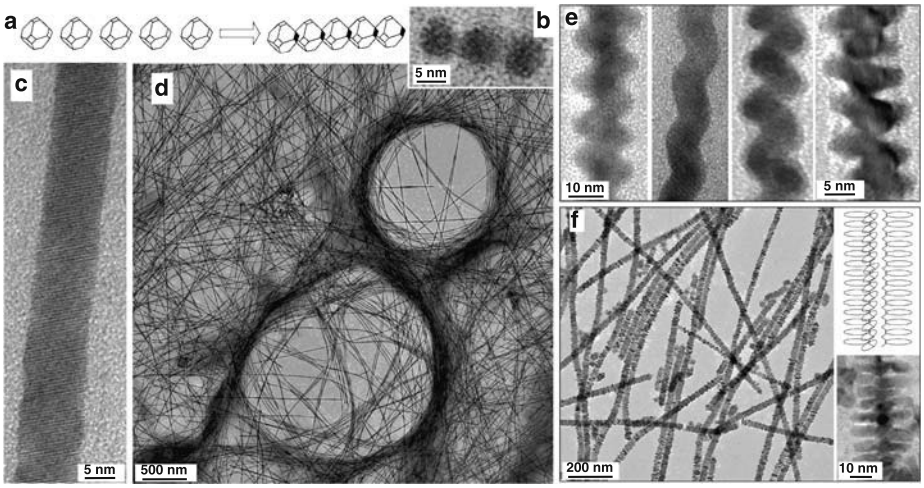

Fig. 5. PbSe nanowires synthesized by one-dimensional assembly and oriented attachment of nanoparticle building blocks. **a** Schematic representation of oriented attachment process. **b** High-resolution TEM image of "trimer" formed at early stage of the reaction. **c** High-resolution and **d** overview TEM images of straight PbSe nanowires. **e** TEM images of zig-zag and helical PbSe nanowires. **f** TEM images and a corresponding scheme of branched PbSe nanowires

Depending on the mutual arrangement of the $\langle 1\,1\,1\rangle$ facets, the whole nanocrystal can either have central symmetry and thus a zero net dipole moment or it can lack central symmetry and possess a dipole moment along the $\langle 1\,0\,0\rangle$, $\langle 1\,1\,0\rangle$, or $\langle 1\,1\,1\rangle$ axes, respectively (Fig. 4d). Assuming a random distribution of polar $\langle 1\,1\,1\rangle$ facets and cuboctahedral shape PbSe, the majority of PbSe nanocrystals ($\sim 89\%$) should have nonzero dipole moments, that drives their oriented attachment.

One-dimensional assembly and oriented attachment of nanoparticle building blocks allow us to obtain large quantities of high quality, catalyst-free semiconductor nanowires (Fig. 5). These nanowires can form stable colloidal dispersions and, therefore, are easy for solution-processing and device integration. Moreover, the nanowire synthesis through oriented attachment produces nanowires with control of wire dimensions and morphology. In addition to straight nanowires, zig-zag, helical, branched, and tapered nanowires as well as single-crystal nanorings could all be prepared by the adjustment of the reaction conditions (Fig. 5). Different nanowire morphologies may be advantageous depending on the potential applications. Straight nanowires with minimal surface roughness may provide the high carrier mobilities necessary for high-performance FETs [31]. On the other hand, the performance of nanowire-based sensors [32, 33] and photovoltaic devices [34] should improve by increasing the wire surface area, i.e., highly branched nanowires may best match these applications. The performance of nanowire-based thermoelectric devices [35, 36] may substantially benefit from the multiple scattering of acoustic phonons in zig-zag and helical nanowires.

2.3 Self-assembly of nanoparticles into two-dimensional structures.

Inorganic nanoparticles can form various structures upon evaporation of carrier

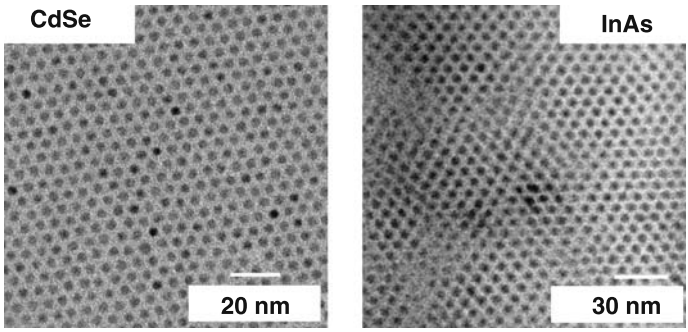

Fig. 6. Examples of two-dimensional ordered arrays of semiconductor nanocrystals viewed in TEM

solvent from a colloidal solution. Depending on nanoparticle concentration, solvent, temperature, substrate, etc., different types of nanoparticle aggregates can be obtained. If solvent and substrate show good wetting properties, dilute solutions of monodisperse nanoparticles can produce long-range ordered two-dimensional superlattices shown in Fig. 6. Such arrays typically show hexagonal packing corresponding to maximal packing density of nanoparticles in 2D and the strongest van der Waals interactions. The spacing between crystallites in the monolayer is determined by the length of the surfactant molecules and can be adjusted by tailoring the capping ligands. The interparticle spacing determines degree of electronic or magnetic coupling between the nanoparticles and plays an important role for design of nanoparticle-based thin-film materials and devices [5, 37].

Formation of nanoparticle films on a substrate induced by solvent evaporation was modeled by Rabani et al. using coarse-grain model of nanoparticle self-assembly [38]. Irreversible evaporation of solvent was considered as a non-equilibrium process. Because of non-equilibrium nature of this process, the nanoparticle assemblies can exhibit complex transitory structures, even when equilibrium fluctuations are mundane [39]. Depending on coverage and mobility of nanoparticles different patterns of nanoparticle aggregates were obtained. Disk-like and ribbon-like morphologies were found to represent different stages of the same growth mechanism [38] as a result of spatially homogeneous solvent evaporation (Fig. 7). When evaporation is heterogeneous in space, the dynamic of self-assembly can be dramatically different and determined by the nucleation and growth of vapor bubbles. If nanoparticles are sufficiently mobile to track the fronts of growing vapor nuclei, the aggregate patterns will be shaped by the structural history of the evaporation. In other words, the distribution of nanoparticle aggregates traces the intersection lines of the colliding vapor nuclei, leading to the network morphologies [38, 39]. Even though coarse-grain model does not take into account hydrodynamic convection flows, film thickness, substrate roughness and non-local interactions, it successfully explains a variety of experimentally observed patterns [38].

Self-assembly of nanoparticles can occur both on solid substrate and liquid surface. Reasonably ordered multilayer films of nanoparticles can be deposited by the different modifications of Langmuir–Blodgett (LB) technique. The LB approach is based on the formation of a monolayer of charged long-chain molecules at the

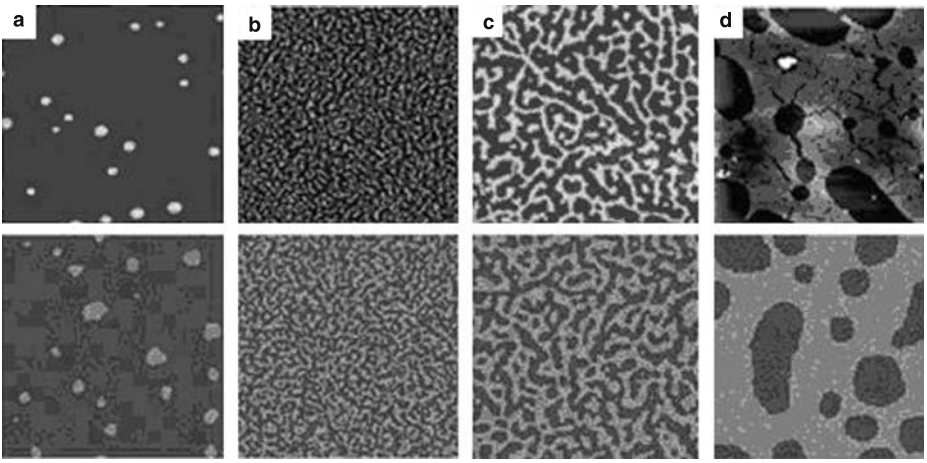

Fig. 7. Self-assembled morphologies resulting from homogeneous evaporation and wetting of nanoparticle domains. The bottom panels demonstrate the coarse-grain model simulations assuming homogeneous evaporation for coverages of 5% **a**, 30% **b**, 40% **c** and 60% **d** and top panels show the experimental results for CdSe nanoparticles with the same coverage. The details of modeling can be found in [38]. Reproduced from [38], © 2003, with permission from Nature Publishing Group

air–liquid interface. These monolayers can be further used for organization of charged particles [1]. It was shown that LB technique can be directly utilized to prepare various phases of organically functionalized nanoparticles by spreading the colloidal solution across the liquid surface of Langmuir trough. Self-assembly of nanoparticles into close-packed 2D or 3D arrays was achieved upon different regimes of film compression [40, 41]. The quality of the Langmuir films is sensitive to particle size distribution, compression pressure, temperature, etc. The great advantage of this method is that the film formed at the air–liquid interface can be further transferred to any substrate. The LB technique was used to deposit monolayers of nearly monodisperse nanometer-size CdSe crystallites onto various substrates. Size-selected CdSe nanocrystals capped with tri-octylphosphine oxide (TOPO) were directly applied onto the water surface of a LB trough and served as the LB-active species [42]. Absorption and luminescence studies of monolayers transferred onto glass slides indicate that the monolayers retain the general optical properties of isolated nanocrystals. Transmission electron micrographs of monolayers on amorphous carbon show the formation of two-dimensional hexagonal close-packed domains. This technique allows us to obtain 2D monolayers of quasi-spherical particles in a controllable and reproducible way. However, the concentration of stacking faults and vacancies in films obtained by LB technique is relatively high [42].

Dynamics of the solvent evaporation is very important and can be varied by changing the temperature and/or solvent. The efficiently screened particle–particle attractions in solution become significant as solvent evaporates. As a result large nanoparticle layers tend to crack upon drying. The appearance of cracks is associated with increasing of van der Waals attractions that shrink the interparticle distances [43]. The compositional inhomogeneity of deposited structures negatively affects the

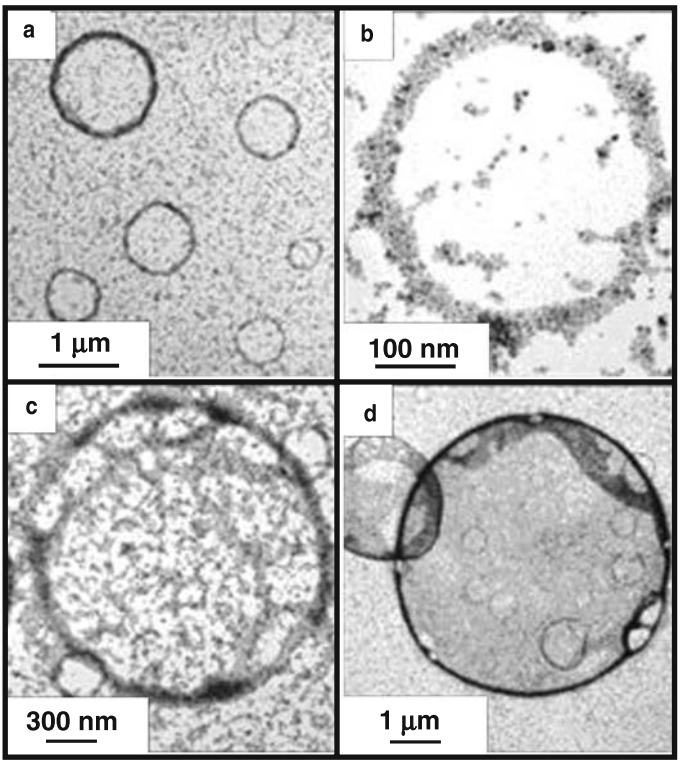

Fig. 8. Various rings obtained from diluted suspensions of CdS nanoparticles. Coverage ratio is 0.5. Reproduced from [44], © 2000, with permission from the American Chemical Society

performance of the self-assembled device. Experimentally, it is hard to avoid the cracking of the drying films. The formed cracks can be filled by infiltration of the deposited nanoparticle structures with extra portion of colloidal solution. However, the deposited layer has to be protected against the dissolution. Striping of the capping ligands from the surface of nanoparticles helps to fix nanoparticles at the substrates. Plasma-, thermo- and chemo-treatments can be used to remove or modify the capping ligands [37].

Controllable solvent evaporation can lead to formation of more sophisticated patterns such as nanoparticle rings, dendrites and islands with radial particle size gradients. Several mechanisms can be responsible for the formation of rings (Fig. 8) [17, 44]. One of the possible explanations of the appearance of micron wide, uniform in size rings consisting of nanoparticles is nucleation and growth of holes in the solvent films completely wetting the substrate. Hole nucleation in an evaporating film can be modeled as substrate-mediated boiling and hole formation can be considered as bubble nucleation in a bulk of superheated liquid with the only difference that holes in thin films are “open” to the vapor above the film [40]. The growth of holes pushes the particles and solvent out toward the “bulk” wet film of colloidal solution. If the nucleation and growth of holes are separated in time, rings uniform in width will be formed. The force acting on the hole rim increases linearly

with the size of the hole, and the number of particles being swept out by the hole area increases quadratically [45]. The concentration of nanoparticles inside the ring is significantly lower as compared to particle concentration outside. In this model the particle–particle attractions are considered not to exceed thermal energies. As a result, particles can be moved until the friction arising from their attraction to the substrate pin the contact line. The resulting hole size depends on particle size and their concentration [46]. In the case of low concentrations, the contact lines of the holes will not be pinned before the "percolation" of the growing holes and compact domains of nanoparticles will be formed. The smaller size of nanoparticles also favors the growth of compact nanoparticle domains: small particles can more easily overcome their static friction [45] and as a result, the pinning size of hole becomes larger than the average distance between holes.

The Marangoni effect can also lead to ring-like nanoparticle patterns. Evaporation of a thin film of volatile solvent can create significant temperature variation between the substrate and the free upper surface leading to the temperature gradient across the film. The interfacial tension depends on the temperature and, as a result, local "hot" and "cold" spots generate low and high interfacial areas pulling the solvent from the warmer to cooler areas. At the same time solvent moves upward to the warmer places in order to compensate the concentration perturbation. This generates a convective flow through the liquid film and leads to the appearance of a network of cells. Inside those the fluid goes up by the center of the cells and goes down by the walls of the cells.

Dimensionless parameter determining the threshold of this dynamic solvent instability is called the Marangoni number (M_a):

$$M_a = -\frac{d\sigma}{dT}\frac{1}{\eta\alpha}L\Delta T \tag{8}$$

where σ is the surface tension (N/m), η is the dynamic viscosity (kg/(s m)), α is the thermal diffusivity (m^2/s), L is the film thickness and ΔT is the temperature difference (°C).

The critical value for the Marangoni number is $M_a = 80$. Below this value interfacial instabilities do not appear. Above 80 different patterns can be generated, depending on the system [47]. Increase in temperature and interfacial tension fluctuations, as well as in the thickness of the liquid film promote the appearance of interfacial instabilities, while fluctuation enhancement is suppressed by thermal diffusivity and dynamic viscosity of the liquid. Marangoni effect was found to be responsible for the formation of ring-like structures and hexagonal networks for a variety of nanoparticles of different shapes [44] (Fig. 8). Systematic study performed by Pileni and co-workers [44] demonstrated that ring formation was related on the evaporation rate of the solvent used to disperse nanoparticles. Replacement of highly volatile hexane with decane, as well as evaporation of hexane solution under the "saturated" vapor of hexane, led to the precipitation of random dispersions of nanoparticles [44].

Dendrites are another interesting example of self-assembled nanoparticle structures. Dendrite-like structures are generated as a result of the interplay between the ordering effect of crystallization, the disordering effect of local orientation fluctu-

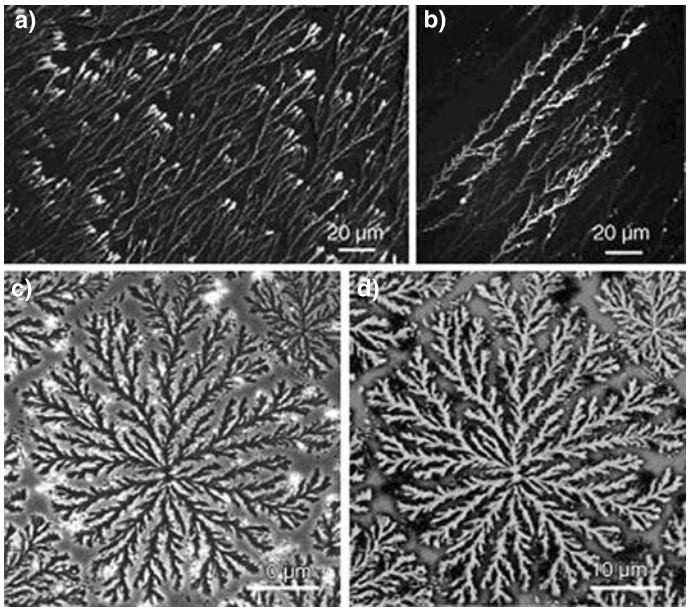

Fig. 9. Phase contrast (**a**, **c**) and fluorescent (**b**, **d**) images of dendrites formed by water-solubilized CdSe/ZnS quantum rods (**a**, **b**) and by quantum dots (**c**, **d**) upon their drying-mediated self-assembly at room temperature at 0.3 mg/mL concentration. Reproduced from [48], © 2006, with permission from Wiley

ations of the nanoparticles and the freezing of the domain edges after complete solvent evaporation [48]. Recently, dendrites consisting of CdSe/ZnS nanodots and nanorods were reported (Fig. 9) [48]. Typically, dendrites formed from nearly spherical nanoparticles consisted of highly luminescent core with six-to-ten branches. Self-assembly of nanorods under the same conditions led to the formation of long, highly asymmetric dendrites with 2–3 branches growing towards the droplet center. The difference in the morphology of nanodot and nanorod dendrite structures can be attributed to stronger dipole–dipole interactions between rods and their shape-related anisotropy [48]. Increase of the particle concentration as well as evaporation temperature was found to cause gradual decrease of the lateral sizes of dendrites and an increase of their thickness.

Some size distribution is always present in nanoparticle samples and this could have a substantial influence on both thermodynamics and kinetics of formation of nanoparticle superlattices. As an example, pair wise van der Waals attraction in a sample of polydisperse nanoparticles is strongly dependent on particle size (Eq. (6)). Attractions between the largest particles are the strongest. As a result they energetically prefer to be clustered together forming characteristic structures where the largest particles at the center are surrounded by smaller particles (Fig. 10a) [17]. This experimental observation has been supported by Monte Carlo calculations performed for a system of particles with mutual attraction described by Eq. (6) (Fig. 10b).

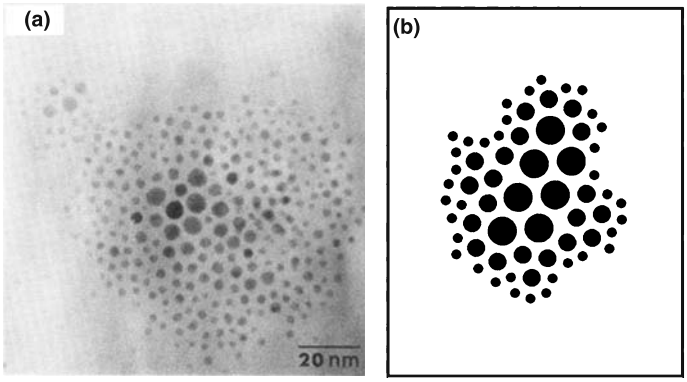

Fig. 10. a TEM micrograph revealing the size-dependent phase separation in polydisperse Au nanocrystals capped with dodecanethiol. **b** Simulated pattern for a system containing 7A, 21B and 36C Au spheres with radii of 1.0, 0.6 and 0.3, respectively. The energy of the system was minimized via Monte Carlo simulated annealing routine. The minimum allowable distance between particle cores is 0.5. Reproduced from [17], © 1995, with permission from American Institute of Physics

Formation of two-dimensional nanoparticle assemblies often occurs at the interfaces, liquid–solid, liquid–air or liquid–liquid. The interface typically plays a role of template directing assembly of nanoparticles in two dimensions. However, Kotov and co-workers recently reported that CdTe nanoparticles stabilized with 2-(dimethylamino)ethanethiol can spontaneously form monolayers of two-dimensional free-floating sheets consisting of individual CdTe nanoparticles in the bulk of solution (Fig. 11) [25]. This very counterintuitive observation has been explained by simultaneous effects of electrostatic interactions arising from both dipole moment

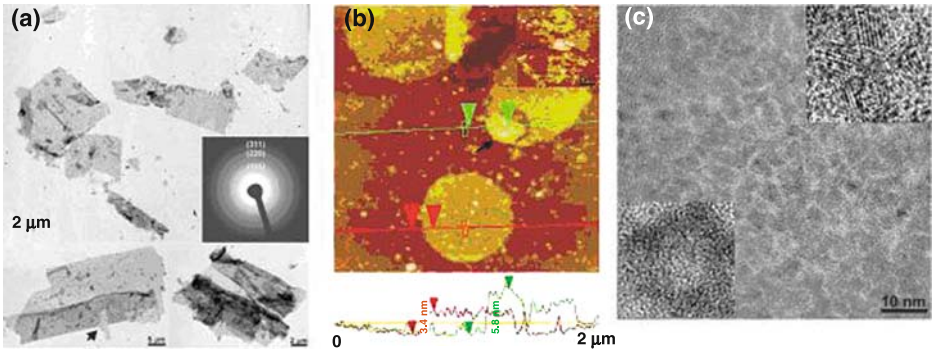

Fig. 11. a TEM images of free-floating films of CdTe NPs. (Inset) Electron diffraction pattern obtained from the films. **b** Tapping-mode AFM and corresponding topography cross sections of the monolayer films on a silica surface. Inset: large-scale AFM image of the films. The morphology of the films is the same for hydrophilic and hydrophobic TEM grids, as well as for AFM images obtained on hydrophilic and hydrophobic Si substrates. **c** High-resolution TEM images of the monolayer films of CdTe NPs. The inset at top right represents a detailed arrangement of single NPs obtained by HRTEM. Each particle has a distinct cubic crystal structure identified from the spacing between adjacent crystal planes inside the NPs equal to 0.38 nm, which corresponds to (111) surfaces of zinc blend CdTe. Inset at bottom left shows characteristic assembled rings of cubic CdTe NPs with zinc blend cubic crystal structure. Reproduced from [25], © 2006, with permission from AAAS

and a small positive particle charge combined with hydrophobic particle–particle interactions. The positive charge of CdTe particles stabilized with 2-(dimethylamino)ethanethiol was estimated to be 1*e* to 3*e*. Monte Carlo simulations confirmed the importance of the "net" charge for the formation of 2D nanoparticle aggregates [25].

2.4 Self-assembly of nanoparticles into three-dimensional superlattices. Nanocrystals can form three-dimensional structures with different degree of short- and long-range ordering. Individual nanoparticles can be brought together as freestanding structures or thin films in two forms: (i) amorphous (glassy) and (ii) crystalline solids. Glassy solids are isotropic materials with only short-range order and randomly oriented nanoparticles (Fig. 12). Close-packed glassy films usually form if the nanoparticles are polydisperse or if the rate of destabilization of a colloidal solution is high (e.g., very fast solvent evaporation) [11]. If colloidal nanoparticles are poorly soluble in a given solvent due to insufficient sterical repulsion or the lack of the capping ligands on nanocrystal surface, no long-range ordered arrays is expected. Also, if repulsive forces dominate particle–particle

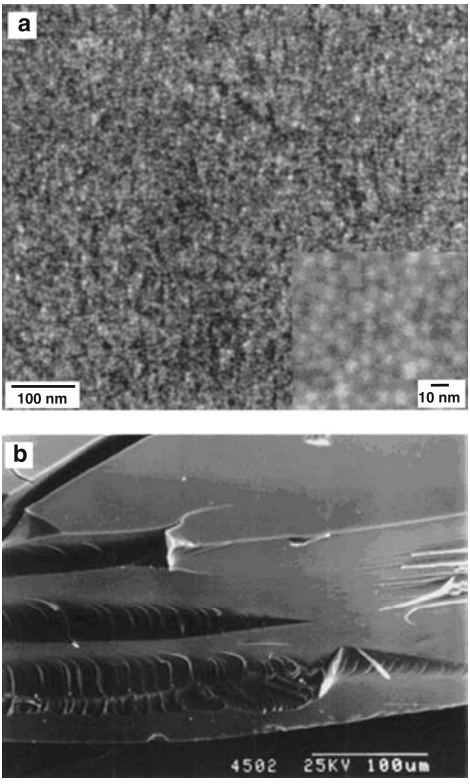

Fig. 12. **a** Low and high (inset) magnification SEM micrographs of a glassy solid prepared from 5.6 nm CdSe nanoparticles. **b** SEM micrograph of the fracture surface from a $\sim 150\,\mu m$ thick glassy solid of 3.8 nm CdSe nanoparticles. The NC solid was imaged by tilting it 45° with respect to the incident electron beam. Reproduced from [11], © 2002, with permission from Annual Reviews

interactions and these interactions are weak, there is no sufficient energy driving the formation of an ordered lattice [11]. As the concentration rises with solvent evaporation, the viscosity of the dispersion increases until it freezes the local structure of nanoparticles in the form of glassy-like solid. High-resolution SEM images (Fig. 12a) demonstrate examples of glassy-like film formed from CdSe nanoparticles. The nanoparticle glass is a brittle material and can fracture under the stress (Fig. 12b) [11]. Even though glassy-like structures allow realizing dense packing of nanoparticles, they are characterized by the absence of compositional uniformity because of the lack of "global" periodicity in particle distribution. In the case of periodic structures the positions of particles and, as a result, chemical composition, are known. This makes periodic nanoparticle structures (e.g., films, colloidal crystals) more attractive for practical applications and fundamental studies of their properties.

Generally, both entropy and isotropic attractive van der Waals forces should favor assembly of spherical particles into the structures with highest packing density such as face centered cubic (*fcc*) and hexagonally close-packed (*hcp*) lattices. In *fcc* and *hcp* lattices hexagonally close-packed layers are shifted with respect to each other in a way that centers of mass in one layer are above the hole in the layer below. This gives three different layer positions marked as A, B and C. As schematically shown in Fig. 13, *hcp* and *fcc* lattices have characteristic ABAB- and ABCABC-type stacking of hexagonally packed nanocrystal layers.

In an ensemble of non-interacting hard spheres entropy can be a sole driving force for the transition from disordered into long-range ordered state. This transition spontaneously occurs when the volume fraction of monodisperse hard spheres exceeds a threshold value of 0.494 [7]. Theoretical calculations and simulations of hard-sphere colloids predict that *fcc* structure should be slightly more stable compared to *hcp* [8, 9]. The free energy difference between these two close-packed structures with identical packing density (~ 0.7405) is very small, $\sim 10^{-3}$ kT per particle. In agreement with this prediction, monodisperse micron-size latex and silica

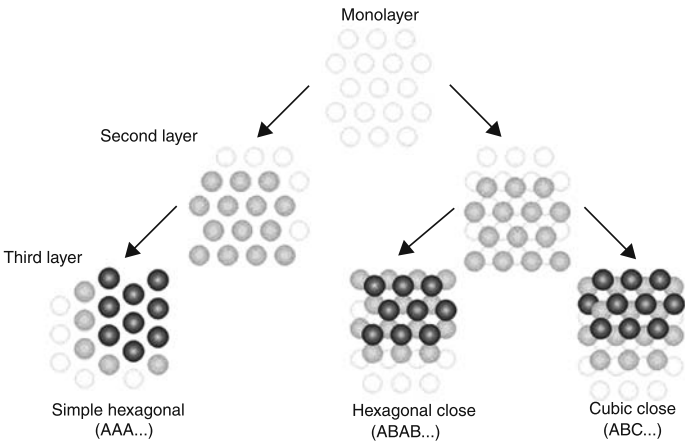

Fig. 13. Schematic depiction of nanoparticle packing in different periodic structures

spheres, whose behavior is similar to hard spheres, exhibit predominantly *fcc* superlattices, also known as synthetic opals, whereas the *hcp* phase does not form [49, 50]. Kinetic factors associated with solvent flow can also play an important role

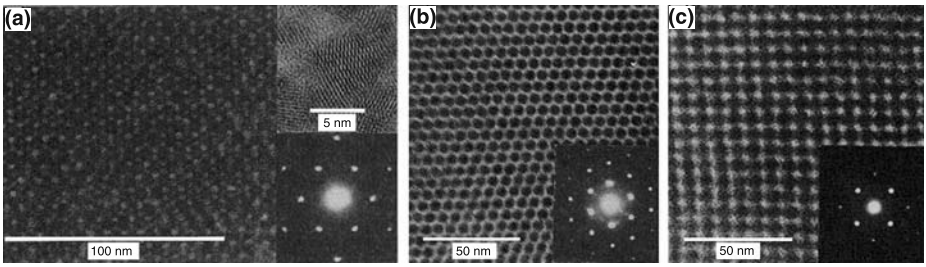

Fig. 14. TEM images and ED patterns of different projections of *fcc* nanoparticle superlattices: **a** ⟨1 1 1⟩-, **b** ⟨1 0 1⟩- and ⟨1 0 0⟩-oriented arrays of 6.4 nm (**a**) and 4.8 nm (**b**, **c**) CdSe nanoparticles, respectively. The lower insets in **a**–**c** show the small-angle ED patterns. The upper inset in **a** is high-resolution image of a single 6.4 nm nanoparticle sitting on the top surface of the array with its (1 1 0) axis parallel to the electron beam and its (0 0 2) axis in the plane of the superlattice. Reproduced from [51], © 1995, with permission from AAAS

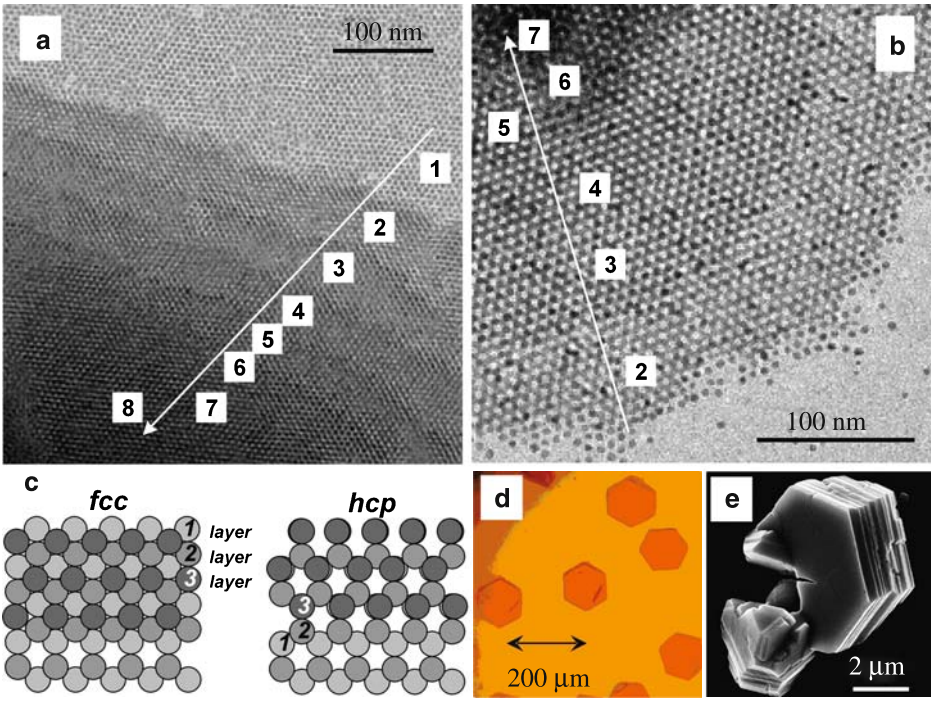

Fig. 15. Nanoparticle superlattices with *hcp* packing symmetry. **a** TEM image of [111] projection of a superlattice self-assembled from CdSe nanocrystals. The numbers highlight nanocrystal layers with ABAB. . . layer stacking, characteristic to the *hcp* lattice. **b** TEM image of an [111] projection of *hcp* superlattice self-assembled from $CoPt_3$ nanocrystals. **c** Scheme showing the difference between [111] projections of *fcc* and *hcp* packing. **d** Optical micrograph of macroscopic 3D superlattices of CdSe nanocrystals faceted as hexagonal platelets, typical for *hcp* lattice. **e** SEM image of 3D superlattice of $CoPt_3$ nanocrystals. Reproduced from [23], © 2007, with permission from American Chemical Society

in determining structure of nanoparticle superlattices, usually favoring the formation of *fcc* phase.

Both *fcc* and *hcp* structures were found in CdSe nanocrystal superlattices (Figs. 14 and 15) [51]. In real nanoparticle superlattices, the effects associated with the slight deviation of nanoparticle shape from spherical, the presence of dipole moments or coupling of higher order multipole moments can influence the relative stabilities of *fcc* and *hcp* phases. As an example, dipolar coupling of nanoparticles in a superlattice can provide higher stability of *hcp* structure compared to *fcc*, due to more favorable dipolar coupling in the *hcp* packing, with odd layers sitting on the top of each other. This explains the experimentally observed formation and stability of *hcp* nanocrystal superlattices (Fig. 15) [23]. The calculations for 5.8 nm CdSe nanocrystals with

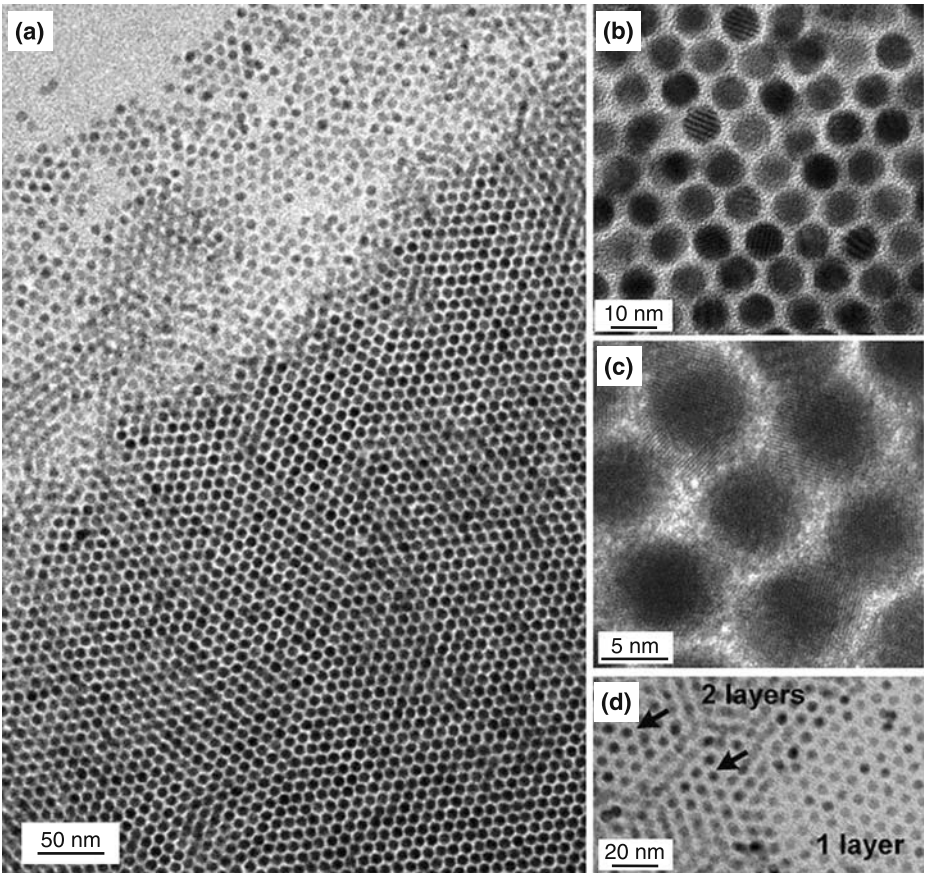

Fig. 16. *shp*-Type superlattices of 7.2 nm PbSe nanocrystals. **a** Overview TEM image showing interface between superlattice and unstructured phase. **b** TEM image showing moiré fringes originating from the diffraction of electrons on nanocrystals with mutually rotated atomic planes and **c** corresponding high-resolution TEM image. **d** TEM image showing formation of the second layer of PbSe nanoparticles with AA layer stacking (i.e., directly above the particles from the first layer). Arrows show hexagonally ordered nanocrystal columns. Reproduced from [23], © 2007, with permission from American Chemical Society

dipole moments of 100 D predict a small ($\sim 1\%$) difference between the binding energies of *fcc* and *hcp* lattices of nanoparticles due to dipolar coupling [23]. These results correlate well with the calculations of the Madelung energies for bulk *fcc* and *hcp* lattices, which predict higher stability of the *hcp* phase in dipolar spheres with ferroelectric ordering [23]. The Madelung energy difference between *hcp* and *fcc*, proportional to μ^2, can overcome the entropic contribution to the free energy, for 5.8 nm nanoparticles the transition from *fcc* to *hcp* superlattice is predicted to occur at $\mu \sim 50$ D at room temperature [23].

Both *fcc* and *hcp* types of packing are very common for nanoparticles of semiconducting and magnetic materials, however, ordering of nanoparticle dipole moments can stabilize superlattices with more open structures. Thus, non-close-packed structures with simple hexagonal packing (*shp*) have been observed for lead chalcogenide nanocrystals [23]. In *shp* lattice, nanocrystals form layers with hexagonal ordering, and these layers assemble one-on-one in the vertical direction (i.e., AAA-type layer stacking) (Fig. 13). It was found that nearly spherical PbSe and PbS nanocrystals with diameters above ~ 7 nm often self-assemble into *shp*-type superlattices shown in Fig. 16. Instead of growing layer-by-layer, these structures form abrupt boundaries with the unstructured phase. Diffraction of electrons in a column of nanocrystals with mutually rotated atomic lattice planes gives rise to rotational moiré fringes, seen in Fig. 16b. The PbSe nanocrystal superlattice exhibits an undistorted hexagonal arrangement of nanocrystal columns, with the angles between the lattice planes very close to 60° what makes them distinctively different from [0 1 1] projections of *fcc* lattice which is always stretched by $\sim 15\%$ in one direction (Fig. 17). The observation of non-close-packed structures self-assembled from spherical particles provides additional evidence that real semiconductor nanocrystals cannot be approximated by hard spheres and possess strong particle–particle interactions. The formation of *shp* structure was explained by considering the interactions between non-local dipoles of individual nanoparticles [23]. In addition to dipoles, higher order moments of charge distribution can also affect the binding energy in nanoparticle superlattices. For example, cuboctahedral PbSe nanocrystals with eight polar $\langle 1\,1\,1 \rangle$ facets can possess high quadrupole and octapole moments [29] that may stabilize other "open" superlattices (e.g., simple cubic) [23].

Perfection of self-assembled structure strongly depends on the superlattice growth conditions. Self-assembly requires that the components either equilibrate between aggregated and non-aggregated states, or adjust their positions relative to each other in an aggregate [1]. The arriving particles must have enough energy and time to find equilibrium superlattice sites on the growing structure. This might be achieved by diffusing on a terrace and along the superlattice step edge. Generally, slow growth is important to obtain highly ordered structures. If new nanoparticles are arriving too fast or stick together irreversibly, they will land on the top of each other and block the diffusion pathways for each other that will lead to the formation of amorphous solid. Tailoring the evaporation conditions by changing the temperature and/or composition of the dispersing media allows us to adjust the destabilization of colloidal solution. For instance, hexane (95%)/octane (5%) solvent mixture leads to the formation of glassy-like structures, while more highly boiling octane (95%)/octanol (5%) media gives long-ranged periodic structures [11]. This approach allows the

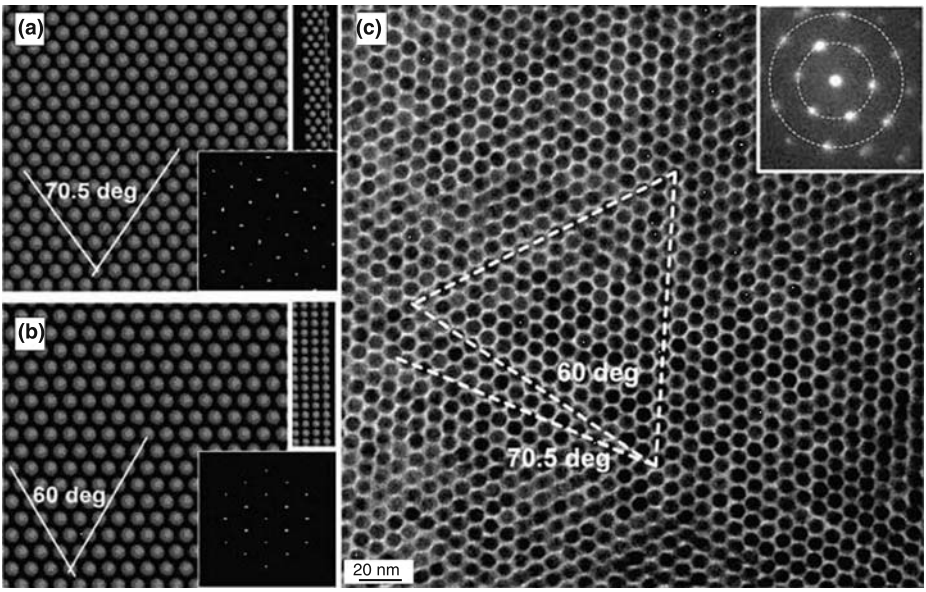

Fig. 17. Modeled **a** [0 1 1] projection of *fcc* lattice and **b** [0 0 1] projection of *shp* lattice. Right bottom insets show FFT of these lattice projections with **a** 2-fold and **b** 6-fold rotational symmetry. Right top insets show side view of the superlattices. **c** TEM image of 7.2 nm PbSe nanocrystal superlattice. The angle between superlattice planes is 60°, typical for *shp* lattice. The inset shows small-angle electron diffraction pattern collected from $6\mu^2$ superlattice area. Reproduced from [23], © 2007, with permission from American Chemical Society

production of three-dimensional NC superlattices coherent over hundreds of microns [51]. Faceted colloidal crystals 5–50 μm in size made from CdSe nanoparticles are shown in the optical micrograph (Fig. 18). The red color of the triangles in the optical micrograph is arising from the optical spectrum for the 5.7 nm CdSe nanoparticle building blocks.

Another approach to create three-dimensional nanoparticle superlattices is controllable oversaturation of a colloidal solution without solvent evaporation. The nanoparticle self-assembly is induced by slow diffusion of a non-solvent into a concentrated solution of nanoparticles (Fig. 19) [52]. The difference in the density of colloidal solution of nanoparticles (e.g., in toluene) and non-solvent (e.g., isopropanol or methanol) provides initial sharp interface between two liquids which slowly interdiffuse. The rate of mixing of the colloidal solution of nanoparticles with non-solvent determines the rate of the destabilization of the former, and hence the rate of the crystallization of nanoparticles. For example, slow diffusion of methanol into toluene solution of monodisperse CdSe nanoparticles induces the spontaneous nucleation and growth of 3D supercrystals (Fig. 20). Both irregular-shaped colloidal crystals with sizes up to 200 μm and perfectly faceted hexagonal colloidal crystals with sizes of about 100 μm have been built from monodisperse CdSe nanocrystals, depending on the conditions of the crystal growth. Irregular shape of colloidal crystals can be a result of faster destabilization of toluene solution of CdSe nanoparticles by methanol that leads to faster nucleation of multiple nuclei which

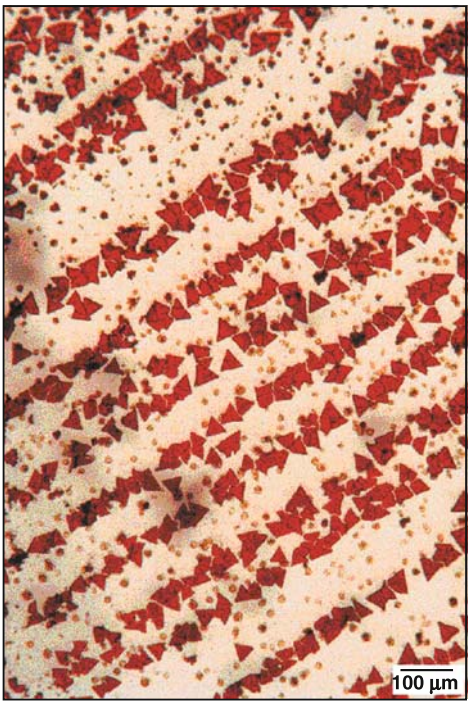

Fig. 18. Optical micrograph of three-dimensional colloidal crystals of 5.7 nm CdSe nanoparticles. The red color of the triangles is characteristic of the size-dependent absorption for the 5.7 nm CdSe nanoparticle building blocks. Reproduced from [11], © 2002, with permission from Annual Reviews

grow and fuse forming large "polycrystalline" crystals consisting of several domains. Isopropanol is a weaker non-solvent compared to methanol and intermixing of isopropanol and toluene results in gentler destabilization of nanoparticle solutions leading to the formation of relatively uniform highly periodic structures [52]. The method of controllable oversaturation of a colloidal solution has been successfully used for growing faceted three-dimensional superlattices of different materials: CdSe [52], FePt [53], $CoPt_3$ [54], PbS [55], and CdSe/ZnS core-shell nanocrystals. The crystals assembled from semiconductor nanocrystals can have various shapes corresponding to terminations by different crystallographic planes (Fig. 21) [55].

The ordering of nanocrystals in superstructures is also observed in SAXS patterns [11] through appearance of sharp reflections in the region of 2Θ angles of ~ 1–15°. Figure 22a shows SAXS patterns measured on superlattices of CdSe nanocrystals of different size. SAXS patterns show a set of reflections that are characteristic for a given symmetry of nanocrystal packing. These reflections can be modeled and assigned to certain crystallographic directions (Fig. 22). The 2Θ positions of small-angle reflections provide information about lattice constant of superlattice unit cell that can be used to calculate center-to-center distance between nearest neighbors. If the size of nanocrystal core is known from independent measurements (e.g., TEM or absorption data), the difference between center-to-center distance and nanocrystal diameter gives information about separation of nanocrystals in the superlattice. The

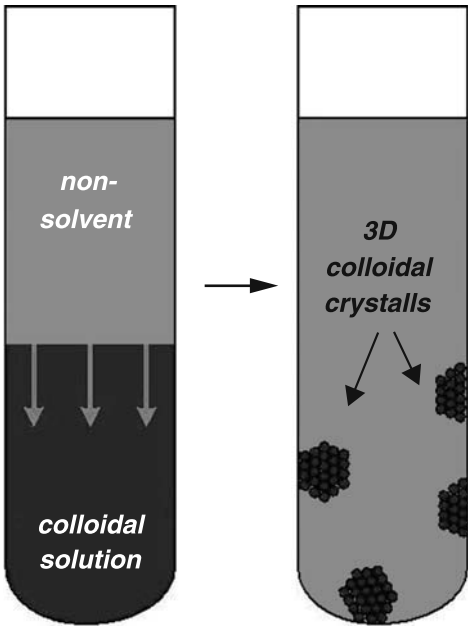

Fig. 19. Controllable oversaturation of a colloidal solution of nanocrystals. Left tube: the non-solvent (methanol) diffuses into a colloidal solution of CdSe nanocrystals in toluene. Right tube: nanocrystal superlattices nucleate and grow on walls of the tube

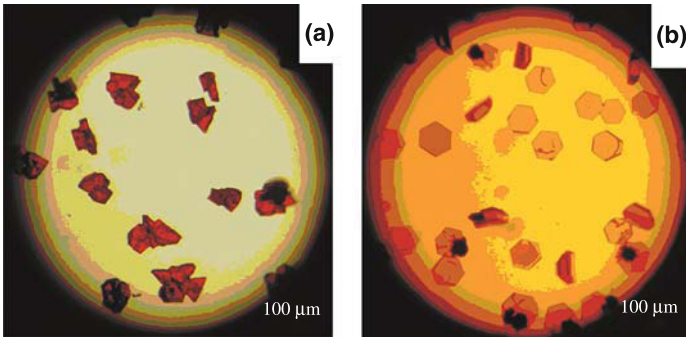

Fig. 20. Optical micrographs of colloidal crystals of CdSe nanocrystals taken by a digital camera through the objective of an optical microscope. **a** Faster nucleation, irregular-shaped crystals. **b** Slower nucleation results in perfectly faceted hexagonal platelets. Reproduced from [52], © 2001, with permission from Wiley

spacing between nanocrystals is determined by the length of the capping ligands and can be adjusted by changing the capping groups (Fig. 22b). The important advantage of SAXS over TEM or SEM is that SAXS data are averaged over large number of nanocrystals, whereas the TEM and SEM data always represent a tiny fraction of nanocrystals in the sample [56].

The wide-angle part of X-ray diffraction patterns corresponds to the diffraction of X-rays on atoms the nanocrystals consist of, and allows the estimation of average size

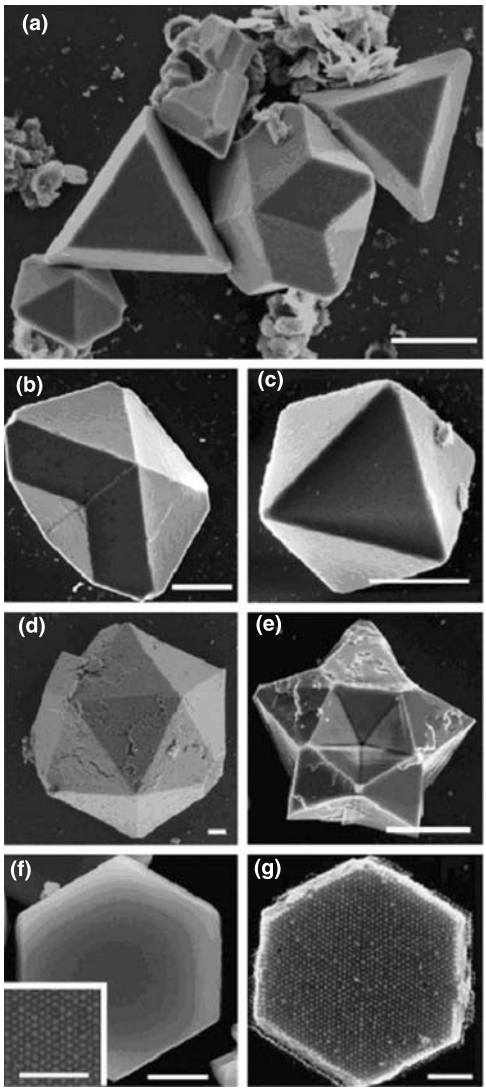

Fig. 21. SEM and HRSEM images of three-dimensional crystals self-assembled from PbS nanoparticles. The scale bars correspond to 1 μm in parts **a–d**, and **f**, 20 μm for part **e**, and 100 nm for parts **g** and the inset of **f**. Reproduced from [55], © 2007, with permission from Oldenbourg Wissenschaftsverlag

of crystalline domains within each nanocrystal. Wide-angle XRD of nanoparticles reveals the internal structure of the average nanocrystal core and permits measurement of nanoparticle size using Debye–Sherrer approximation [56]. Experimentally, WAXS patterns not just demonstrate broadening associated with finite particle size but also provide information about the lattice alignment of individual nanoparticles within superlattice. The ordering and orientation of the individual nanoparticles in the superlattice can be evidenced by the dramatic enhancement in the intensity obtained from certain crystallographic reflections. Thus $\sim$90% of CdSe nanopar-

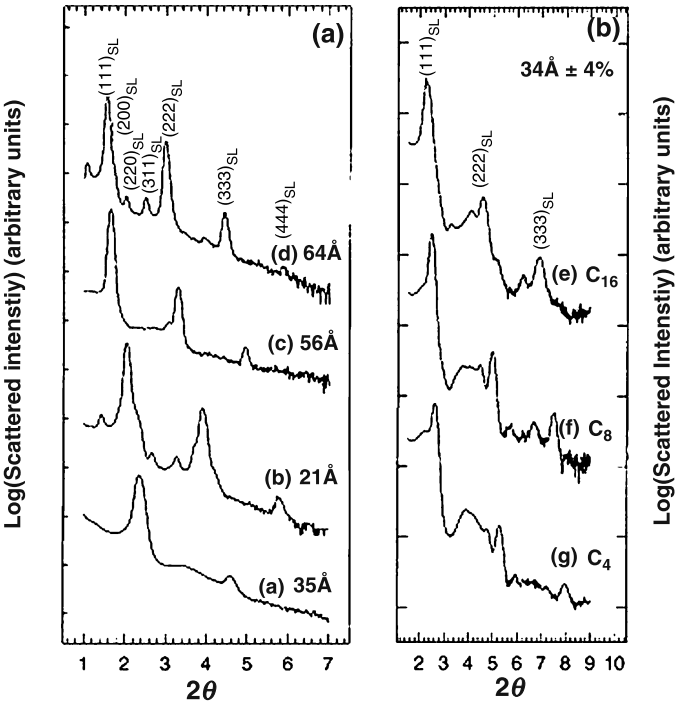

Fig. 22. **a** SAXS patterns for superlattices prepared from CdSe nanocrystals ranging from 3.5 to 6.4 nm in diameter. The *fcc* superlattice reflections are indicated at the top of **a**. **b** SAXS patterns of highly ordered thin films prepared from 3.4 nm CdSe nanocrystals with (e) tricetylphosphate, giving a 1.7 nm inter particle spacing; with (f) the native tri-octylphosphine chalcogenide, giving a 1.1 nm spacing; and with (g) tri-butylphosphine oxide, giving a 0.7 nm spacing. Reproduced from [11], © 2002, with permission from Annual Reviews

ticles were found to be aligned with (1 1 0) planes of the wurtzite *c*-axis in the plane of the substrate (Fig. 23a). The same information can be obtained from wide-angle electron diffraction (Fig. 23b). Preferential alignment of lattices of individual nanoparticles leads to the strong modulation of the diffraction pattern. Preferential alignment of nanoparticles within superlattice can be associated with the fact that during the superlattice growth, the individual nanoparticles may align themselves in order to maximize their attractive interaction (e.g., van der Waals and dipolar) with the substrate and neighboring nanoparticles [57]. In the case of glassy thin films wide-angle pattern is represented by continuous rings and consisted with a randomly oriented ensemble of nanoparticles.

Some size distribution is always present in nanoparticle samples and this could have a substantial influence on both thermodynamics and kinetics of formation of nanoparticle superlattices. Experiments on crystallization of latex particles that can be modeled as hard spheres showed the suppression of crystal formation in suspensions with polydispersity exceeding 12% [58]. From our experiments on self-assembly of semiconductor nanoparticles from non-polar solvents we found that particle size distribution is one of the key parameters determining if crystallization

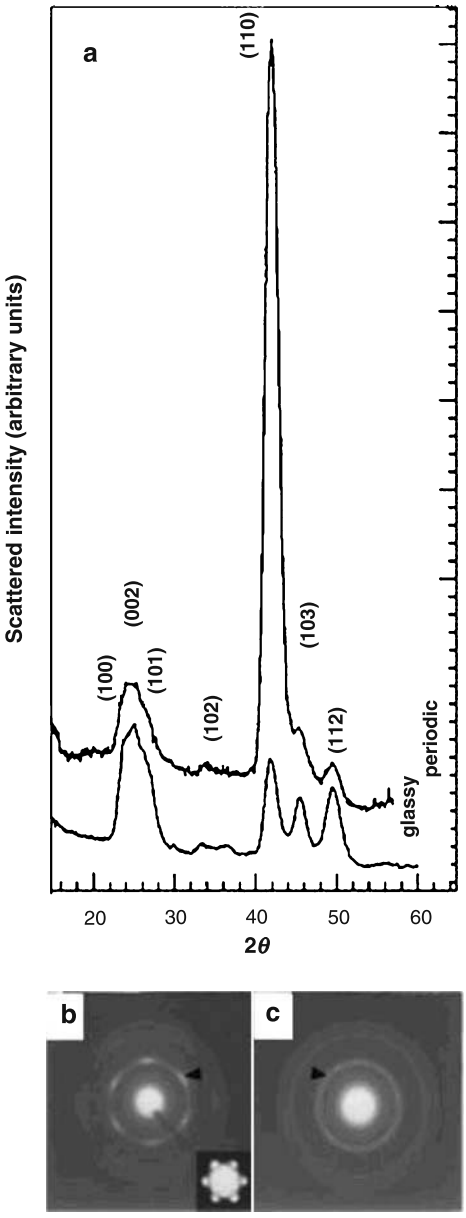

Fig. 23. a WAXS for an oriented periodic and a glassy thin film prepared from 6.4 nm CdSe nanoparticles assembled in *fcc* superlattice. **b**, **c** Wide-angle electron diffraction patterns from a $\sim 2\,\mu$m area with *fcc* and randomly packed nanoparticles, respectively. Reproduced from [11], © 2002, with permission from Annual Reviews

occurs or not. The best particle size distribution achieved for sub-10 nm semiconductor nanoparticles is $\sim$4–6% which is sufficient to obtain periodic superlattices over tens of microns [11, 51, 52]. Increase in polydispersity up to $\sim$10–12% results

in the significant decrease in the size of ordered domains. Monte Carlo simulations performed for hard spheres revealed that the nucleation barrier is independent of the polydispersities below 5% [59]. Increase in particle size distribution above 5% leads to the rapid increase of the nucleation barrier and formation of critical nuclei is suppressed. Calculations also demonstrated that crystallization is not observed in hard-sphere suspensions with a polydispersity greater than 12% and under these conditions the colloidal glass is truly amorphous [59].

Any crystal is characterized by certain concentration of defects, such as vacancies, interstitials, dislocations, etc. Numerical calculations showed that equilibrium concentration of interstitials in hard-sphere colloidal crystals is almost undetectable [60]. It can be associated with high mobility of interstitials. Being trapped during the crystal growth, interstitials diffuse rapidly to the crystal surface. On the other hand, the concentration of vacancies was found to be three orders of magnitude higher than the concentration of interstitials [60]. Size distribution can also affect the concentration of stacking faults and point defects. Concentration of interstitials in crystals grown from polydisperse colloids can be up to six orders of magnitude higher than in crystals formed from monodisperse colloids [61]. Such a dramatic increase in interstitial concentration was attributed to the presence of small particles that have an increasing probability of fitting in a hole of the underlying crystalline lattice. Calculations demonstrated that the concentration of interstitial depends sensitively on the tail of the size distribution in the liquid phase [61]. Control over defects in crystalline nanoparticle superlattice is important for many device applications. However, to date there is no established techniques for quantitative analysis of defect concentrations in nanoparticle superstructures.

3. Self-assembly of anisotropic nanoparticles

The recent progress in colloidal synthesis of inorganic nanomaterials established robust techniques for tailoring not only the size but also the shape of semiconductor nanocrystals. For example, the shape of CdSe nanocrystals can be tuned from nearly spherical to rod-, disk-, arrow-, rise-, teardrop- and tetrapod-like [62, 63]. PbSe nanocrystals can be synthesized in form of spherical particles as well as cubes and octahedrons [29]. These shape-controlled nanocrystals attract great interest because they cannot be treated as purely “zero-dimensional” quantum dots [64]. Thus, CdSe nanorods can have the aspect ratio up to $\sim$30 and exhibit the properties being intermediate to that of 0D and 1D objects [65]. Highly anisotropic inorganic semiconductor nanostructures are perspective candidates for photovoltaic applications because they can exhibit benefits of quantum-confined systems without compromising facile charge separation and transport. The photogenerated charges can immediately be harvested and transported within the 1D unit. Semiconductor nanorods have tunable linearly polarized photoluminescence and anisotropic nonlinear optical properties that opens up the possibility of using them in electro optical devices such as flat panel displays, polarized light-emitting devices, etc. Tuned aspect ratios (length/diameter), replaceable surface capping molecules and diversity in composition of semiconductor nanorods make them an ideal system to study the fundamental aspects of self-assembly of anisotropic particles.

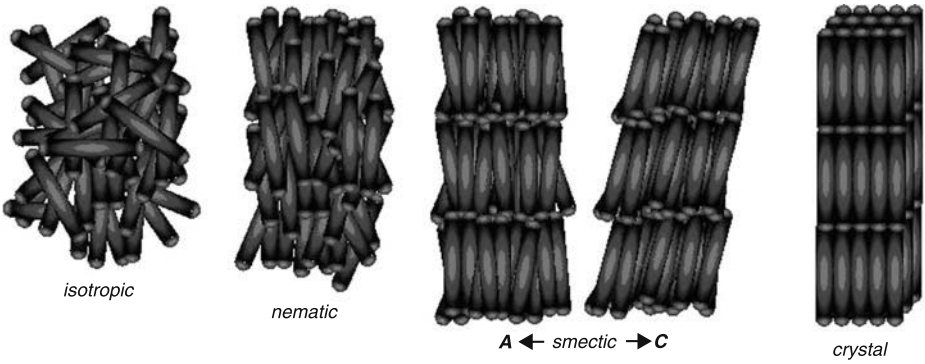

Fig. 24. Typical assemblies of rod-like particles with different degrees of ordering

This section is primarily focused on self-assembly of nanorods into periodic structures which are of interest for many technologically important applications [66]. The phase behavior of rods was extensively studied both experimentally and theoretically. Onsager's theory as well as extensive computer simulations [67–69] predict formation of a series of orientationally and/or positionally ordered phases upon assembly of anisotropic particles. The most of theoretical models and numerical calculations consider rods as non-interacting hard spherocylinders. It is known that a collection of rods can exist in at least four stable phases: isotropic fluid, nematic liquid crystals, crystalline solid and a smectic (mainly A) phase [70] (Fig. 24). Isotropic crystals are represented by randomly oriented rods with no orientational and positional order. There is a large variety of different types and degrees of positional and orientational ordering. The most common are nematic, smectic-A, and smectic-C phases. Nematic liquid crystal is the simplest liquid crystalline phase characterized by lower degree of orientational order than smectic phase and it also has no positional order. In smectic phases the rods form defined layers being positionally ordered along one direction. The rods are typically oriented either normally to the layers (smectic-A phase) or tilted to the same angle (smectic-C phase, Fig. 24). In crystalline structures the rods show both positional and orientational ordering. Typically, in crystalline phase the rods have the same arrangement as spherical particles packed into the simple hexagonal lattice discussed in the previous section: the rods in each hexagonally close-packed layer are located directly above and below the rods from adjacent top and bottom layers (Fig. 24).

Self-assembly of rods is less entropically favorable compared to spherical particles because it requires both positional and orientational ordering of individual rods. Recent computer simulations predict stunted crystal growth in ensembles of hard spherocylinders because of kinetic "self-poisoning" of lamellar crystal nuclei [71]. Simulations predict that single-layered lamellar crystallite forms at the early nucleation stage. However, the top and bottom surfaces of this crystallite prefer to be covered with rods that align parallel to the surface. The preference of rods to lie flat on the lamella surface facilitates lateral growth of the layer, however, it makes growth of the top/bottom surface difficult. Numerical study demonstrates that the rods have to overcome a barrier of $\sim 1.5\,kT$ per particle to stand up on the surface and align

with the director while the lateral growth of nanorod layer is easy [71]. Real semiconductor nanorods have strong longitudinal dipole moments [15]. Pairing of the dipole moments can significantly contribute to thermodynamics and kinetics of self-assembly process. Monte Carlo simulations for hard spherocylinders demonstrate that longitudinal dipoles can stabilize the layered smectic phases due to antiparallel side-by-side dipole pairing within a layer and between the adjacent layers [72].

At low concentrations, colloidal solution of CdSe nanorods is isotropic and shows polarization independent extinction, no birefringent patterns are observed. Evaporation of solvent (e.g., cyclohexane) causes gradual increase of the nanorod concentration and at certain point birefringent liquid crystalline phase appears. Figure 25 demonstrates two stages following the evaporation of cyclohexane from a solution of CdSe nanorods with a length of 40 nm and a width of 4 nm. First, the isotropic phase undergoes a phase transition breaking into multiple droplets. The intense red color of these droplets, called tactoids, indicates the high concentration of CdSe nanorods in the droplets. The droplets are birefringent – the anisotropic refractive index of the liquid crystalline phase alters the polarization of transmitted light, leading to light and dark patterns on the micron scale viewed in optical microscope at crossed polarization [73]. The variations in the intensity of the transmitted light through the

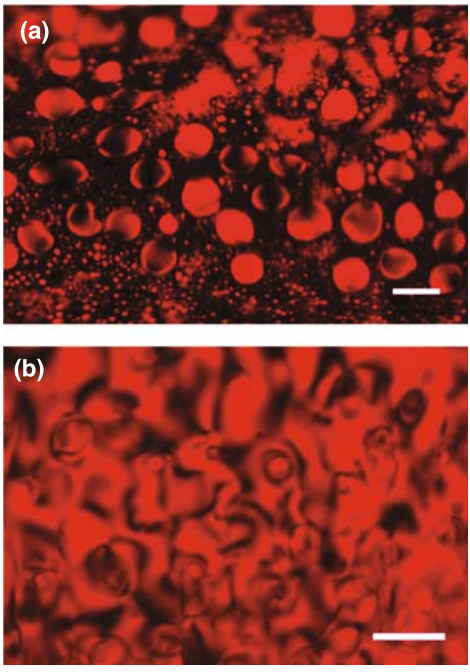

Fig. 25. Optical micrographs obtained for CdSe nanorods with the length of 40 nm and the width of 4 nm dispersed in cyclohexane at different stages of solvent evaporation: **a** phase-separated droplets of concentrated CdSe nanorods in cyclohexane and **b** Schlieren texture. The images were obtained by illumination with linearly polarized white light and detected at crossed polarization. The red color is due to strong band edge absorption of the CdSe nanorods. The scale bars are 20 μm. Reproduced from [73],

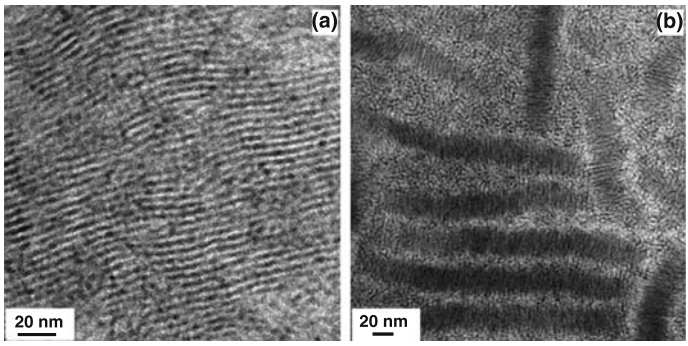

Fig. 26. Assemblies with (**a**) nematic and (**b**) smectic ordering of 22 nm × 3.5 nm CdSe nanorods

droplets indicate alignment of the rods within each droplet. The patterns are generally dipolar (Fig. 25a). At later stage of solvent evaporation so-called Schlieren structures characteristic to nematic phase form. Dark thread-like brushes are observed sticking out from some singular points. The singular points (disclinations) have been identified as the positions where the alignment direction of the nanorods is not well defined. The dark brushes are due to the particles with alignment parallel to either of the polarizers. When the sample is rotated, these singular points remain fixed but the dark brushes move around them. When one end of the capillary tube is lifted, the patterns flow and deform easily, suggesting the fluidity of the birefringent phase [73].

Fast evaporation of concentrated toluene solutions of monodisperse CdSe nanorods leads to the formation of solids with nematic order (Fig. 26a) [74]. However, if a high boiling solvent such as butyl ether is added to the concentrated nanorod solution followed by drying at 40–60°C under reduced pressure, long tracks of CdSe nanorods would be stacked side by side. At higher concentrations, these tracks align parallel to each other, resulting in smectic-A ordered superstructures (Fig. 26b). Experimentally, nanorods with high aspect ratios were found to be more difficult to self-assemble into structures with orientational and/or positional order [75].

Slow destabilization of toluene solution of CdSe nanorods by the diffusion of a non-solvent (e.g., ethanol, isopropanol, etc.) allows us to obtain $\sim$10–50 μm large droplet-like aggregates (Fig. 27a, b). Sonication in ethanol breaks the droplet-like aggregates into sheets (Fig. 27c). HRSEM investigation revealed that these sheets consist of CdSe nanorods packed into long-range ordered crystalline phase (Fig. 27d). The nanorod aggregates shown in Fig. 27a and b exhibit characteristic birefringence, called Maltese crosses (Fig. 28a–c). The simultaneous appearance of Maltese crosses and concentric rings can be explained if the layer-by-layer growth results in a texture where smectically ordered layers are separated by ledges as shown in Fig. 28f. In vicinity of the ledges, nanorods are tilted with respect to layer planes as shown in Fig. 28f and rotate polarization of incident light [74]. The glassy films of CdSe nanorods prepared by fast deposition from a hexane solution exhibit neither Maltese crosses nor concentric rings (Fig. 28d, e). Similar polarized optical micrographs are observed for spherulite textures. Growth of a spherulite originates from a

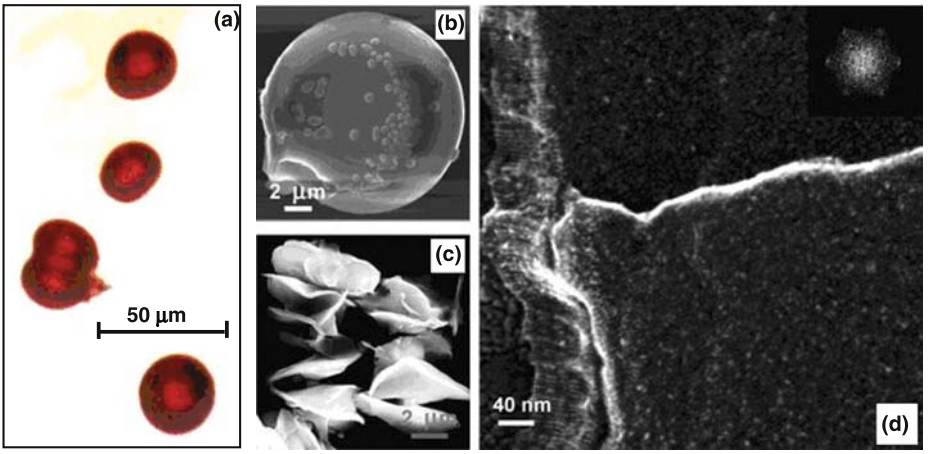

Fig. 27. **a** Optical micrograph of self-assembled aggregates consisting of 18 nm × 3 nm CdSe nanorods. **b** SEM image of an assembly of 22 nm × 3.5 nm CdSe nanorods. **c** Sonication of the nanorod assemblies results in their cleavage in several flat sheets. **d** High-resolution SEM image showing internal packing of CdSe nanorods inside the sheets. Vertical columns of nanorods at the edge of the superlattice show ordering in longitudinal direction. Inset: FFT from selected area of top surface of the nanorod sheet shown in frame **d** demonstrates hexagonal ordering of the nanorods within the layers. On the left, part of the image the ITO substrate can be seen. Reproduced from [74], © 2004, with permission from American Chemical Society

single nucleus (lamellae) followed by uniform growth in three dimensions to form ball-like structures [76]. In the case of a liquid crystal with spherulitic texture, the director rotates around the center of spherulite resulting in a cross-like extinction "Maltese cross", which occurs along the polarization axes of the polarizers. Spherulites of polyethylene and some other polymers exhibit similar concentric extinction rings (radial banding) usually assigned to lamellar twisting along the radial direction during crystal growth [77].

Another interesting example of nanorod assemblies is based on highly luminescent CdSe/CdS heterostructured nanorods [74, 75, 78]. Self-assembled CdSe/CdS nanorod solids (Fig. 29) exhibit strong, stable PL under UV excitation. CdSe/CdS heterostructures are known to be very efficient harvesters of short wavelength light because the CdS part provides large extinction below 500 nm [78]. The photogenerated carriers in the CdS rod are efficiently captured in the CdSe core within $\sim$5 ps. The CdSe/CdS heterostructure nanorods emit in the spectral region where only the CdSe core can reabsorb the emitted light [79]. The extinction coefficients in this spectral region are relatively small. This means that reabsorption in CdSe/CdS heterostructure nanorod solids is considerably smaller than reabsorption in CdSe or any other single-phase nanorod solids. This makes CdSe/CdS nanorods particularly interesting for solid-state luminescence applications such as phosphors, light-emitting diodes and lasers, as well as for detectors and for light harvesting applications. CdSe/CdS nanorods deposited from concentrated toluene solutions preferentially self-assemble into smectic-A and highly periodic hexagonally packed layers (Fig. 29). These layers are oriented perpendicular to the substrate and typically grow laterally rather than in third dimension. CdSe/CdS nanorods can form aligned

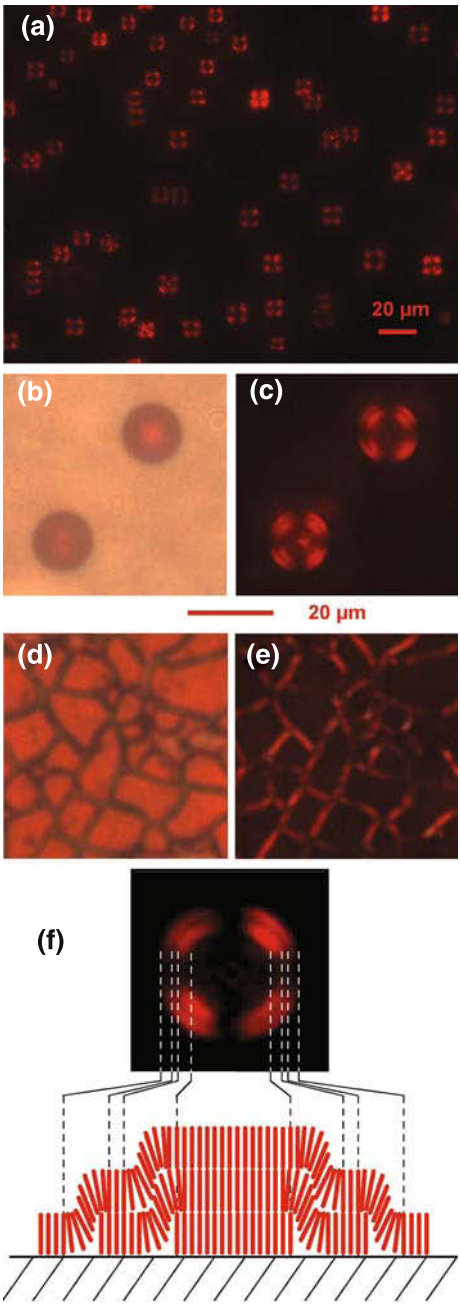

Fig. 28. **a** Optical micrograph of assemblies of 22 nm × 3.5 nm CdSe nanorods viewed between crossed polarizers. Optical micrographs of self-assembled nanorods observed without (**b**) and with (**c**) crossed polarizers at higher magnification. Optical micrographs of a glassy film of CdSe nanorods observed without (**d**) and with (**e**) crossed polarizers. **f** Scheme showing a possible packing of nanorods in the assemblies that is consistent with simultaneous appearance of Maltese crosses and concentric rings. Reproduced from [74], © 2006, with permission from American Chemical Society

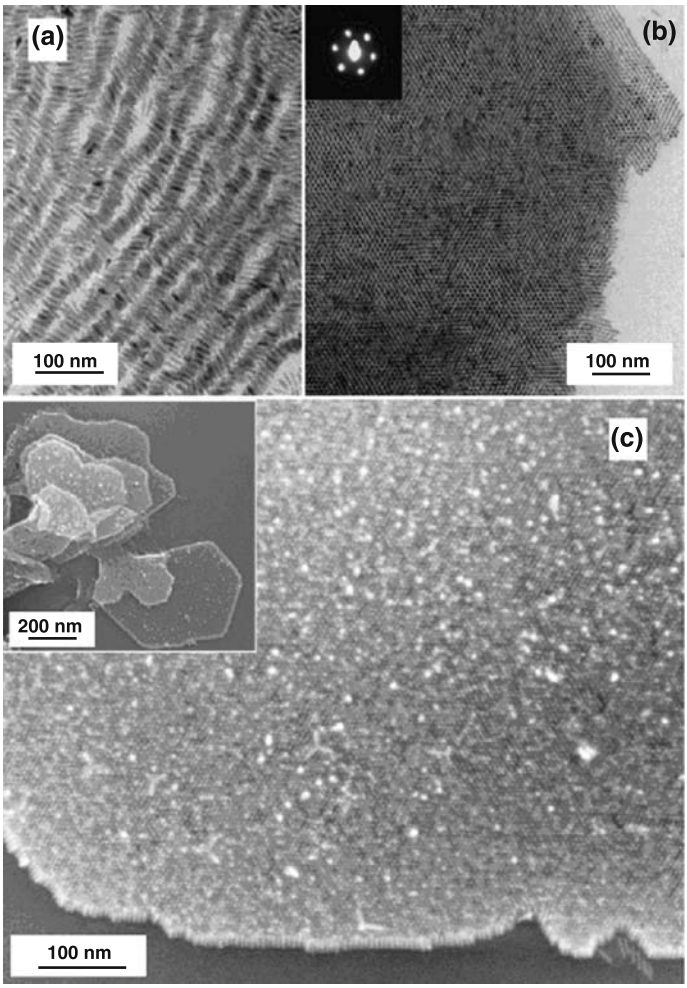

Fig. 29. Self-assembly of 24 nm × 5.2 nm CdSe/CdS nanorods. **a** TEM image of a superstructure with smectic-A ordering. **b** TEM image of a superlattice with simple hexagonal packing of nanorods assembled perpendicular to the substrate. Inset shows electron diffraction from a superlattice domain. **c** HRSEM image of CdSe/CdS nanorods assembled perpendicular to the substrate (silicon wafer). Inset shows layer-by-layer growth of a nanorods superlattice. Reproduced from [78], © 2007, with permission from American Chemical Society

structures floating at the surface of water. Regular patters of vertically stacked nanorods were obtained by evaporating concentrated toluene solution of CdSe/CdS nanorods at the surface of water [75]. The nanorods form hexagonally close-packed monolayers. The AAA stacking of monolayers results in the growth of crystalline phase with high positional and orientational order [75].

Evaporation of nanorod solutions in the presence of external electric field facilitates alignment of individual nanorods and is favorable for the formation of nanorod superlattices [75, 80]. The electric field interacts with nanorod dipole moments, providing high orientational order in the final structures. For example,

evaporation of toluene solution of 30 nm × 5 nm CdS nanorods in electric field (1 V/μm) leads to close-packed structures where all nanorods align along the field [80]. DC electric field was also used to align CdSe/CdS nanorods. The use of high concentrations of CdSe/CdS nanorods allowed us to grow large unidirectionally aligned superstructures with nematic and smectic ordering (Fig. 30).

The recent progress in synthesis of nanostructures with complex morphologies such as, e.g., CdTe and CdSe/CdS nanotetrapods [78, 81] with well-controlled nanoscale dimensions opens up the possibility of new kinds of self-assembled

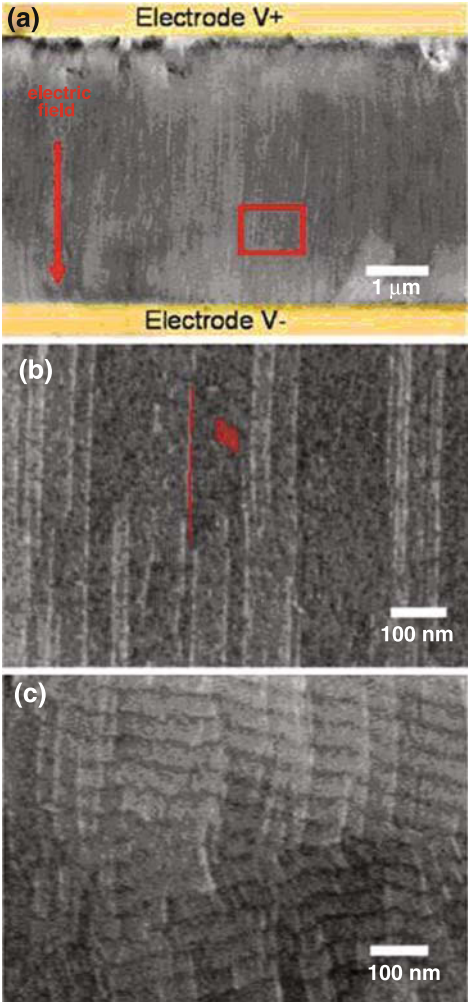

Fig. 30. Lateral alignment of nanorods with electric fields. **a–c** SEM images showing aligned arrays of nanorods with an aspect ratio of 10. The red arrow indicates the direction of the electric field that was applied during the evaporation of the nanorod solution, and the red square marks the region that is displayed in **a**. **b** Micrometer size area where the individual rods can be resolved. Some rods are highlighted in red as a guide to the eye. **c** Zoom that displays an area of nanorods assembled in ribbon-like structures. Reproduced from [75], © 2007, with permission from American Chemical Society

structures. For example, according to theoretical predictions tetrapods with identical arms can assemble into cubatic phase if no kinetic arrest occurs [82]. Cubatic phase is a special case of the biaxial nematic phase with two mutually perpendicular preferred axes.

4. Multicomponent nanoparticle assemblies

The ability to mix and match different nanoparticles and assemble them systematically into ordered binary superlattices, with precisely controlled stoichiometry and symmetry, extends the analogy to multifunctional nanocomposites constituting "nanoparticle compounds". Binary nanocrystal superlattices (BNSLs) raise the possibility of combining the properties of individual components with new properties that arise from the interactions between the nanocrystals. Binary mixtures naturally provide a much richer class of compositions and structures as compared to the monodisperse nanoparticles. When two types of particles cocrystallize, their individual assembly tendencies must adjust themselves to space constrains. They must meet, as well as possible, the requirement of certain geometrical principles. Many theoretical studies have been focused on predicting the probability of the formation of various ordered binary structures and comparison of their stability [83–86]. In the simplest approach, the formation of a binary assembly of hard spheres is expected only if its packing density exceeds the packing density of single-component crystals in *fcc* or in *hcp* structure (~ 0.7405) [86]. This mechanistic space-filling principle formulated by Murray and Sanders is still very useful and allows us to predict the behavior of hard non-interacting particles in binary mixtures. The particle size ratio ($\gamma = R_{small}/R_{large}$) and relative concentrations are considered as the factors determining structure of binary assemblies. In the case of hard spheres, a binary superlattice can form only if its entropy is higher than the sum of entropies of separated *fcc*-packed small and large spheres. Taking into account geometrical considerations, we can expect the formation of superlattices isostructural with NaCl, $NaZn_{13}$, and AlB_2. Detailed computer simulations show that the formation of NaCl-, AlB_2-, and $NaZn_{13}$-type structures of hard spheres can be driven by entropy alone without any specific energetic interactions between the particles [83, 84, 87]. Indeed, $NaZn_{13}$- and AlB_2-type assemblies of silica particles were found in natural Brazilian opals [87] and could be grown from latex spheres [88, 89]. At the same time, the lattices of hard spheres with CsCl, zinc blend, wurtzite structures, as well as any lattices with AB_3, AB_4, and AB_5 stoichiometries were predicted to be unstable for any particle size ratio. Table 2 summarizes the predicted ranges of stability for different hard-sphere binary superlattices. One can see that stable binary lattices usually have the packing density exceeding the packing density of *fcc* and *hcp* lattices (~ 0.7405). This is in agreement with a simple scheme: the higher packing density is, the larger is the excluded volume and, in turn, the higher entropy of the system can be achieved during crystallization of the superlattice [87]. However, the intrinsic entropy of binary superlattice also affects its stability. For example, the maximum packing density of $NaZn_{13}$-type superlattice is slightly below 0.74, whereas the detailed entropy calculations predict stability of this structure in a rather broad range of γ (Table 2) [90].

Table 2. Maximum packing density and range of stability calculated for binary lattices of non-interacting hard spheres. Reproduced from [12], © 2006, with permission from American Chemical Society

Stoichiometry	Type of structure	Maximum packing density (γ)	Range of stability	References
AB	NaCl	0.793 (0.414)	Below 0.458	[26]
			$0.2 \leqslant \gamma \leqslant 0.42$	[24]
	NiAs	0.793 (~ 0.4)	~ 0.4	[57]
	CsCl	0.729, unstable	0.732	[58]
AB_2	AlB_2	0.778 (0.58)	$0.482 \leqslant \gamma \leqslant 0.624$	[26]
			$0.42 \leqslant \gamma \leqslant 0.59$	[24]
	Laves phases – hexagonal: $MgZn_2$, $MgNi_2$: cubic $MgCu_2$	0.71 (0.813), unstable	$0.606 \leqslant \gamma \leqslant 0.952$	[26]
	CaF_2	0.757, unstable	0.225	[24]
A	$NaZn_{13}$ (*ico*-AB_{13})	0.738 (0.58)	$0.54 \leqslant \gamma \leqslant 0.61$	[24]
			$0.474 \leqslant \gamma \leqslant 0.626$	[22, 23]
B	*ico*-AB_{13}, with some size distribution for B spheres	Above 0.755	$0.537 \leqslant \gamma \leqslant 0.583$	[26]
	cub-AB13	0.700 (0.565)	Unstable	[26]

In contrast to these predictions, an amazing variety of BNSLs can self-assemble from colloidal solutions of nearly spherical nanoparticles of different materials (Fig. 31). Coherently packed domains extend up to 10 μm in lateral dimensions and can display well defined facets. In many cases several BNSL structures form simultaneously on the same substrate and under identical experimental conditions [12, 91]. The same nanoparticle mixture can assemble into BNSLs with very different stoichiometry and packing symmetry. Figure 32 shows 11 different BNSL structures prepared from the same batches of 6.2 nm PbSe and 3.0 nm Pd nanoparticles. In general, BNSLs tolerate much broader γ ranges than hard spheres. For example, Fig. 33 shows AlB_2-type BNSLs assembled from different combinations of PbSe, PbS, Au, Ag, Pd, Fe_2O_3, $CoPt_3$ and Bi nanoparticles in a broad γ-range. We also observed BNSLs structures that we could not assign to certain intermetallic compounds. Two of these structures are shown in Fig. 32. The observed structural diversity of BNSLs defies traditional expectations, and shows the great potential of modular self-assembly at the nanoscale. The formation of binary structures with packing density significantly lower than the density of single-phase *fcc* packing (0.7405) rules out entropy as the main driving force for nanoparticle ordering. Experimentally, $\sim$ 5–8% distribution in nanoparticle size of individual nanoparticles was sufficient to grow binary superlattices with dimensions of several microns. Notably smaller fragments ($\sim 400\,nm^2$) of binary superlattices can be obtained from solutions of nanoparticles with polydispersity of $\sim$ 10–12% SD. However, suppression of crystallization from mixtures containing particles with broad size distribution ($\geqslant$ 14% SD) was observed.

Three-dimensional descriptions of the superlattices can be developed by surveying large regions of the samples, to categorize all the crystal orientations, and recording a series of 2D projections down the major symmetry axes. Tilting of the samples allows observation of additional orientations not expressed in the plan view

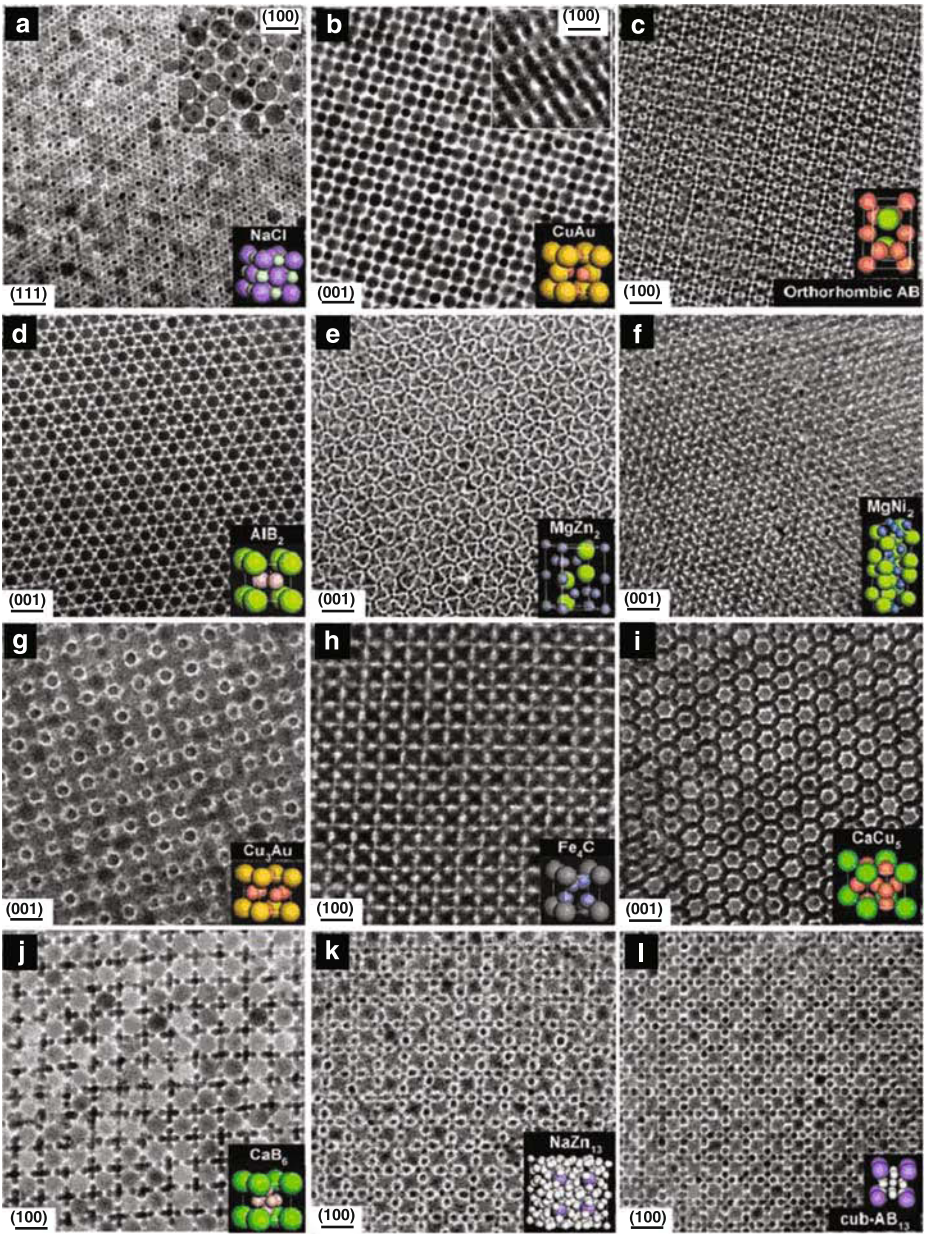

Fig. 31. TEM images of the characteristic projections of the binary superlattices, self-assembled from different nanoparticles, and modeled unit cells (insets) of the corresponding three-dimensional structures. The superlattices are assembled from **a** 13.4 nm γ-Fe_2O_3 and 5.0 nm Au; **b** 7.6 nm PbSe and 5.0 nm Au; **c** 6.2 nm PbSe and 3.0 nm Pd; **d** 6.7 nm PbS and 3.0 nm Pd; **e** 6.2 nm PbSe and 3.0 nm Pd; **f** 5.8 nm PbSe and 3.0 nm Pd; **g** 7.2 nm PbSe and 4.2 nm Ag; **h** 6.2 nm PbSe and 3.0 nm Pd; **i** 7.2 nm PbSe and 5.0 nm Au; **j** 13.4 nm γ-Fe_2O_3 and 5.0 nm Au; **k** 7.2 nm PbSe and 4.2 nm Ag; **l** 6.2 nm PbSe and 3.0 nm Pd nanoparticles. Scale bars: **a**–**c**, **e**, **f**, and **i**–**l**, 20 nm; **d**, **g**, and **h**, 10 nm. The lattice projection is labeled in each panel above the scale bar. Reproduced from [91], © 2006, with permission from Nature Publishing Group

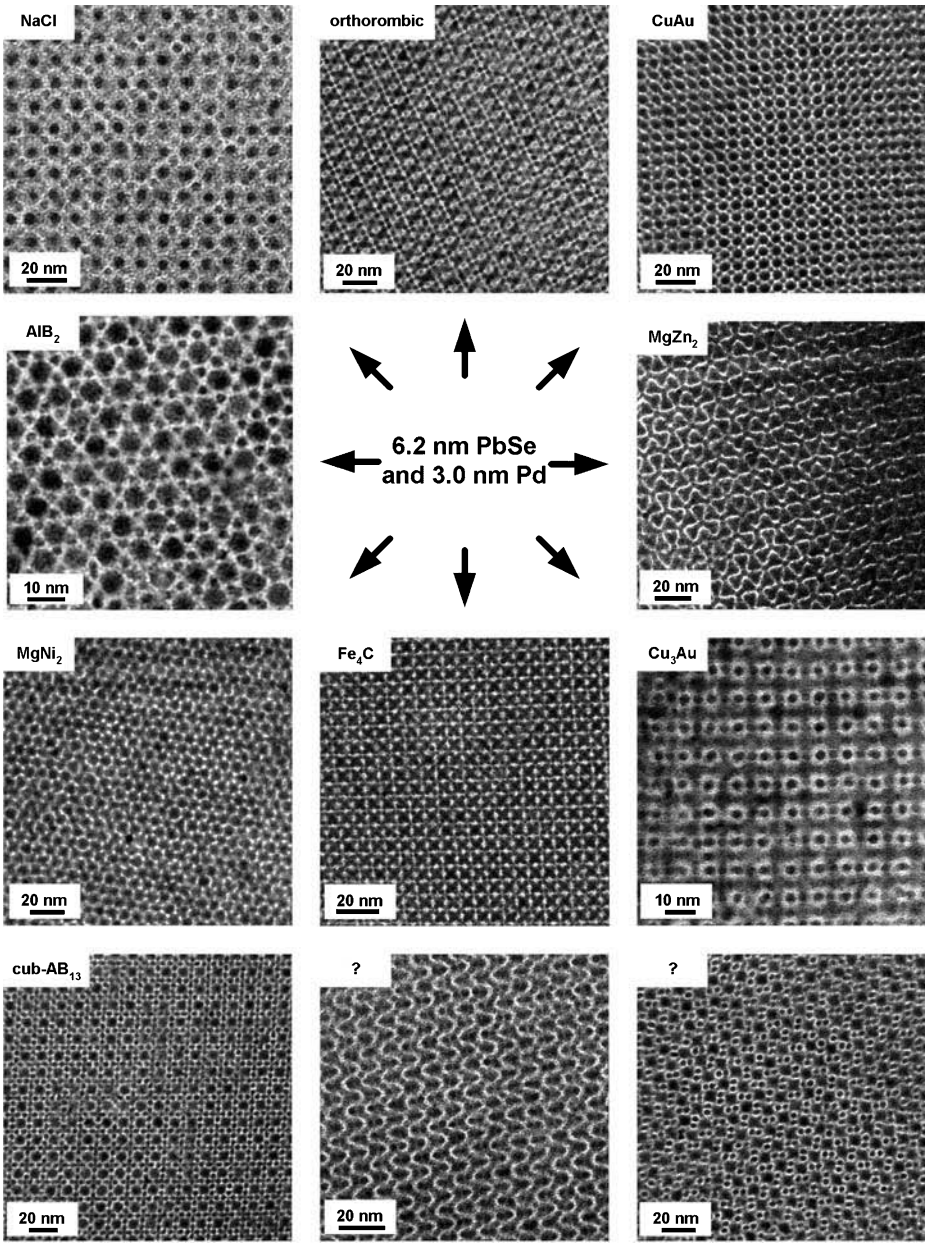

Fig. 32. TEM images of different binary superlattices self-assembled from the same batches of 6.2 nm PbSe and 3.0 nm Pd nanoparticles. Reproduced from [91], © 2006, with permission from Nature Publishing Group

images of the films. In many cases the analysis of series of these 2D lattice projections resulted in a single-crystal structure. To assign the observed structures to crystallographic space groups we built 3D lattice models for the 180 most common

space groups using Accelrys MS Modeling 3.1 software. The TEM images were compared with simulated projections to match the symmetry of the superlattices. We also performed a comparison of experimental small-angle electron diffraction patterns taken over larger areas, and the 2D Fourier transformation power spectra of real-space TEM images and the FFT power spectra of the simulated projections to assure consistency.

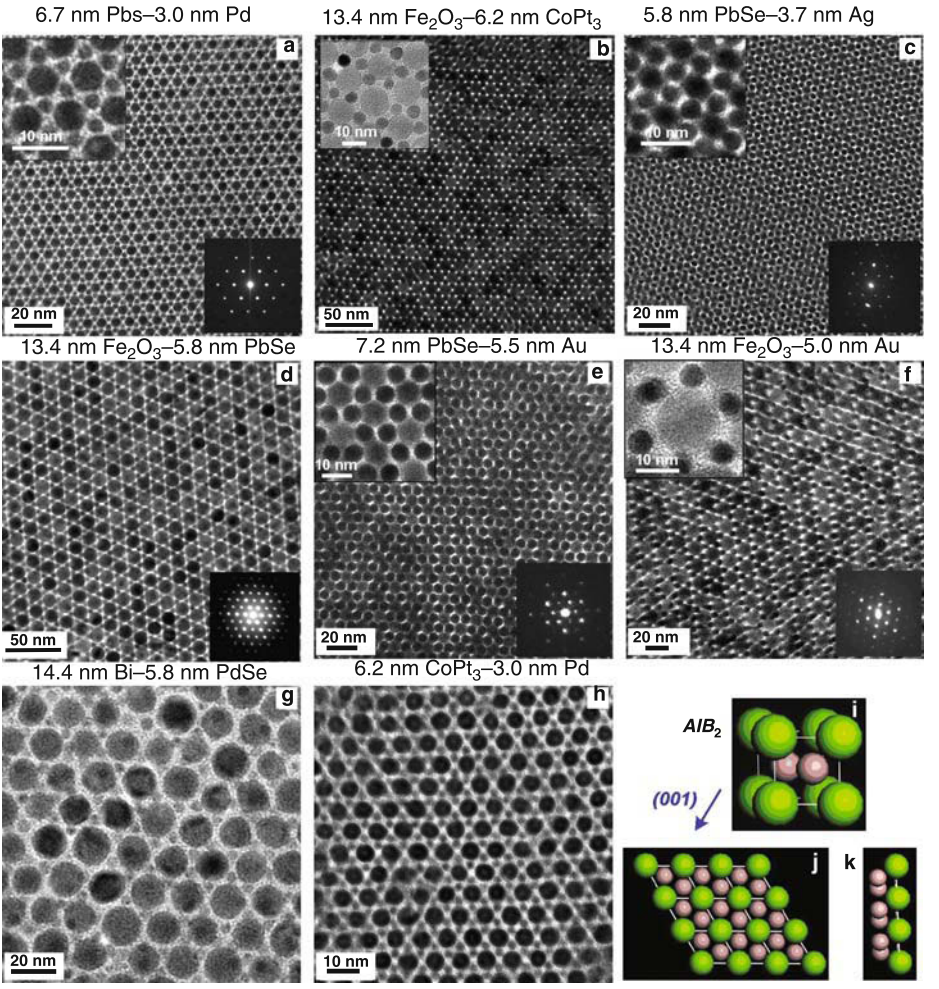

Fig. 33. **a**–**h** TEM micrographs of (0 0 1) planes of binary superlattices isostructural with AlB_2. Top left insets in **a**–**c**, **e** and **f** show the arrangement of NPs in AlB_2-type superlattices at higher magnification. Bottom right insets show small-angle ED patterns measured along the (0 0 1) projection. **i** A unit cell of AlB_2 lattice. **j** Depiction of the (0 0 1) plane. **k** Depiction of minimum number of nanoparticle layers along the (0 0 1) direction necessary to reproduce the observed experimental patterns. The ratio of particle radii (γ) for the reported AlB_2-type binary superlattices varied from 0.43 to 0.79. The γ-range of stability for AlB_2-type packing of hard spheres is shown in Table 2. Reproduced from [91], © 2006, with permission from the American Chemical Society

Theoretical predictions developed for hard spheres fail in the case of real nanoparticles because they cannot be approximated by non-interacting spheres. The combination of space-filling principle and soft (Coulomb) interparticle interactions can generate a rather complex phase diagram, as it has been recently demonstrated for binary superlattices of charged PMMA beads [92]. Crystalline nanoparticles cannot be considered as non-interacting because they undergo strong attractive van der Waals and repulsive sterical interactions [12]. However van der Waals, sterical or dipolar interparticle interactions are not sufficient to explain why these low-density BNSLs form, instead of their constituents separating into single-component superlattices. It was found that opposite electrical charges on nanoparticles can impart a specific affinity of one type of particle (e.g., dodecanethiol-capped Au, Ag, Pd) for another (e.g., PbSe, PbS, Fe_2O_3, $CoPt_3$ capped with long-chain carboxylic acids). If nanoparticles are oppositely charged, the Coulomb potential stabilizes the BNSL while destabilizing the single-component superlattices. The electrical charges can exist on sterically stabilized nanoparticles even in non-polar solvents [13]. Figure 34 shows the distribution of electrophoretic mobilities within a colloidal solution of PbSe and Au nanoparticles. The electrical charge (Z, in units of e) of a spherical

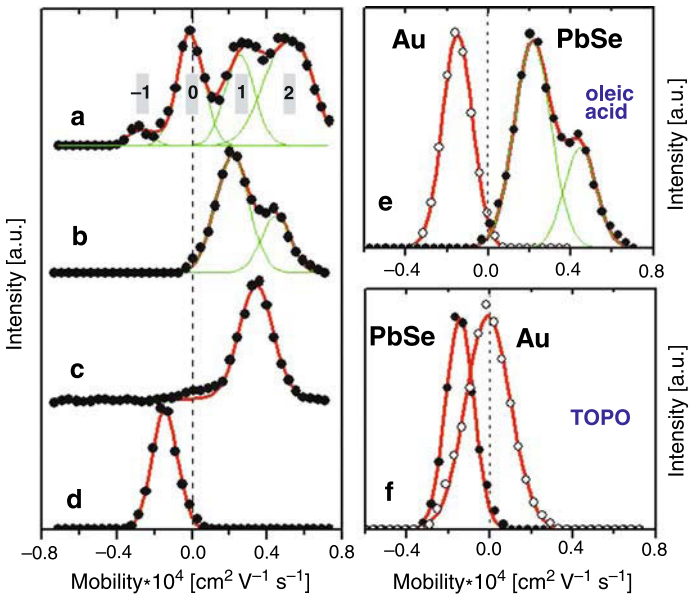

Fig. 34. Electrophoretic mobility of PbSe and Au nanocrystals in chloroform. **a–d** Distribution of electrophoretic mobility for 7.2 nm PbSe nanocrystals. **a** PbSe nanocrystals washed to remove excess of capping ligands. The grey bars show mobilities predicted for nanocrystals with charges of −1, 0, 1 and 2 (in units of e). **b–d** Electrophoretic mobility of PbSe nanocrystals in the presence of **b** 0.02 M oleic acid, **c** 0.06 M oleic acid and **d** 0.05 M tri-*n*-octylphosphine oxide. **e**, **f** Comparison of electrophoretic mobilities of 7.2 nm PbSe and 4.8 nm Au nanocrystals in the presence of **e** 0.02 M oleic acid and **f** 0.05 M tri-*n*-octylphosphine oxide. a.u., arbitrary units. Reproduced from [91], © 2006, with permission from Nature Publishing Group

particle in a low-dielectric solvent can be calculated from the electrophoretic mobility (μ_e) expressed as

$$\mu_e = \frac{Ze}{3\pi\eta a} \tag{9}$$

where η is the viscosity of the solvent and a is the hydrodynamic diameter of a particle [93]. With $a = 10\,\text{nm}$, we obtain $\mu_e \sim 0.27 \times 10^{-4}\ Z\,\text{cm}^2\,\text{V}^{-1}\,\text{s}^{-1}$. These calculated values agree well with the peaks in the experimental mobility distribution for 7.2 nm diameter PbSe nanocrystals in chloroform shown in Fig. 34a. Due to the organic coating (oleic acid) the effective hydrodynamic radius of PbSe nanocrystals extends beyond the crystalline core by 1–2 nm, depending on the density of surface coverage. This observation indicates the presence of particles with charges $-e$, 0, e and $2e$ in a colloidal solution of monodisperse PbSe nanocrystals. The charges on PbSe nanocrystals can be altered by adding surfactant molecules like carboxylic acids and tri-alkylphosphine oxide. Addition of oleic acid increases the population of positively charged PbSe nanocrystals at the expense of the negatively charged and neutral nanocrystals. Depending on the amount of acid added, the majority of nanocrystals can be adjusted to have either one or two positive charges (Fig. 34b, c). Addition of oleic acid increases viscosity of solution, causing the peaks to shift towards lower mobility (compare Fig. 34a–c). The addition of TOPO increases the population of negatively charged PbSe nanocrystals and reduces the concentration of positively charged nanocrystals (Fig. 34d). Surveys of many samples revealed that the additives reliably shifted the distribution of charge states; however, the initial proportion of particles in each charge state was dependent on the sample processing [91]. After addition of oleic acid, the most Au nanoparticles become negatively charged (Fig. 34e), whereas the addition of TOPO neutralizes Au nanoparticles (Fig. 34f). The charges on PbSe and Au nanoparticles could originate from deviations in nanocrystal stoichiometry and adsorption/desorption of charged capping ligands. In the presence of oleic acid, PbSe and Au nanoparticles are oppositely charged (Fig. 34e). The Coulomb potential between two oppositely charged nanoparticles ($Z = \pm 1$) separated by 10 nm of a solvent like chloroform is comparable with kT at room temperature, and solutions of mixed PbSe and metal nanoparticles retain stability for several weeks. The relatively small interparticle potential favors annealing of the BNSLs as they grow. For a NaCl-type BNSL with $Z_+ = 1, Z_- = -1$ and the nearest-neighbor distance $R_0 = 11.5\,\text{nm}$ (Fig. 31c), the Coulomb binding energy per unit cell is estimated to be

$$U_{\text{Coul}} \approx -\frac{MZ_+Z_-e^2}{4\pi\varepsilon_0 R_0} \sim -0.2\,\text{eV} \tag{10}$$

(or $\sim -8kT$ at the superlattice growth temperature, 50°C), where $M = 1.7476$ is the Madelung constant. The contribution from the Coulomb binding energy is comparable to the van der Waals attractive energy expected in a NaCl-type BNSL [22]. In an AB_x BNSL where A and B hold opposite charges, the Coulomb potential per AB_x "molecule" is $U_{\text{Coul}} \sim -\alpha + \beta\,(xZ_- + Z_+)^2 N^{2/3}$ where α and β are positive constants and N is the number of assembled nanoparticles [91]. Coulomb energy determines the stoichiometry of the growing BNSL. An extended three-dimensional BNSL can

form only if the positive and negative charges compensate each other. If during growth the BNSL accumulates non-compensated charge, eventually U_{Coul} changes sign from negative to positive and the growth is self-limiting. The superlattice nucleation stage should be less sensitive to the Coulomb interactions. Indeed, many small domains with different BNSL structure can simultaneously nucleate on the same substrate, but their size does not exceed $\sim 10^2$ nanoparticles [12]. Only one or two structures grow to larger length scales ($\sim 10^6$ to 10^8 particles). BNSLs with many particles per unit cell (e.g., AB_4, AB_5, AB_6, AB_{13}) might form when both negatively charged and neutral Au nanoparticles are incorporated into the structure. The presence of differently charged nanoparticles in the colloidal solutions (Fig. 34a) could also contribute to the simultaneous formation of different BNSLs.

Tuning the charge state of the nanoparticles allows us to direct the self-assembly process. Reproducible switching between different BNSL structures has been achieved by adding small amounts of carboxylic acids, TOPO or dodecylamine to colloidal solutions of PbSe (PbS, Fe_2O_3, etc.) and metal (Au, Ag, Pd) nanocrystals. Figure 35 demonstrates how these additives direct the formation of specific BNSL structures. Combining native solutions of 6.2 nm PbSe and 3.0 nm Pd nanoparticles (particle concentration ratio: $\sim$1:5) results in the formation of several BNSL structures with $MgZn_2$ and *cub*-AB_{13} dominating. However, the same nanoparticles assemble into orthorhombic AB- and AlB_2-type superlattices after adding oleic acid (Fig. 35a) and into $NaZn_{13}$ or *cub*-AB_{13} BNSLs after the addition of dodecylamine or TOPO, respectively (Fig. 35b). In the AB_{13}-type BNSL metal particles assemble into icosahedral ($NaZn_{13}$) or cuboctahedral (*cub*-AB_{13}) clusters, with each large PbSe particle surrounded by 24 metal spheres at the vertices of a snub cube [9]. In the presence of TOPO the metal nanoparticles are neutral (Fig. 34f), favoring formation of the Pd_{13} (Au_{13}, Ag_{13}) clusters. The clusters of metal nanoparticles in turn provide screening of the charges on PbSe nanocrystals in the AB_{13}-type BNSL.

Surveys of many samples show that the addition of a carboxylic acid to solutions of PbSe–Pd, PbSe–Au, PbSe–Ag and PbSe–Fe_2O_3 nanocrystals results in either AB or AB_2 superlattices (Fig. 35c, e), while the addition of TOPO to mixtures of the same nanoparticles favors growth of AB_{13} (if $\gamma \leqslant 0.65$) or AB_5 (if $\gamma \geqslant 0.65$) BNSLs (Fig. 35d, f). Thus the space-filling principles and particle charging work in combination to determine the structure. Adjusting the relative concentration of A and B particles can be used as an additional tool with which to control the BNSL structure. For example, in presence of TOPO AB_4 or AB_5 BNSLs can form when the A:B ratio is $\sim$1:1 while exclusively AB_{13} forms in the presence of excess B particles.

BNSLs can exhibit various effects of preferential nanoparticle orientation. Preferred orientation of the atomic lattices of individual nanocrystals packed into a superlattice can be studied by wide-angle selected area electron diffraction (SAED). Randomly oriented nanocrystals result in uniform diffraction rings in wide-angle SAED patterns as shown in Fig. 36a for a superlattice of 13.4 nm Fe_2O_3 nanoparticles. In contrast, the wide-angle X-ray scattering from Fe_2O_3 nanoparticles packed into the NaCl-type BNSL with 5.5 nm Au nanoparticles (Fig. 36d) appears as a series of arcs rather than continuous rings. These arcs originate from the preferential orientation of Fe_2O_3 nanoparticles in the superlattice. Preferential orientation can sometimes be observed in *fcc* single-component superlattices if nanoparticle shape

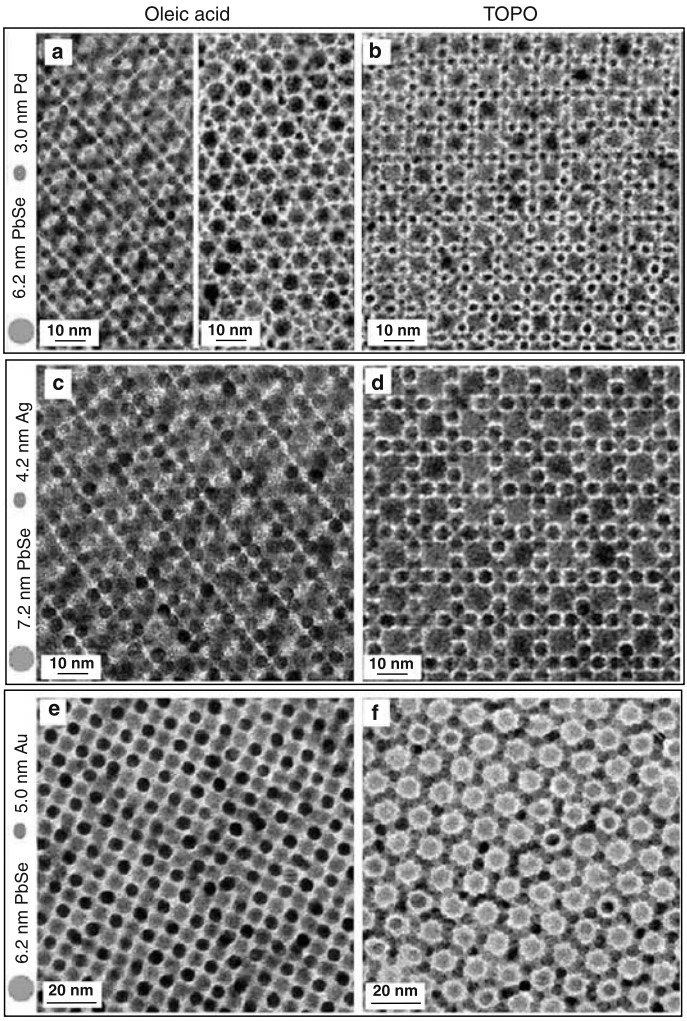

Fig. 35. TEM images of binary superlattices self-assembled in the presence of 4 mM oleic acid (left column) and 6 mM tri-*n*-octylphosphine oxide (right column). **a** 6.2 nm PbSe and 3.0 nm Pd nanoparticles self-assembled into orthorhombic AB- and AlB_2-type BNSLs, and (**b**) into $NaZn_{13}$-type BNSL. **c**, **d** 7.2 nm PbSe and 4.2 nm Ag nanoparticles self-assembled into orthorhombic AB and cuboctahedral AB_{13} BNSLs, respectively. **e**, **f** 6.2 nm PbSe and 5.0 nm Au nanoparticles self-assembled into CuAu- and $CaCu_5$-type BNSLs, respectively. Reproduced from [91], © 2006, with permission from Nature Publishing Group

deviates from spherical due to faceting [11]. Figure 36b, c shows examples of preferential orientation in *fcc* arrays of PbSe nanocrystals.

Single-component *fcc* and *hcp* superlattices of nanocrystals usually show unidirectional orientation of atomic lattices while BNSLs can allow more complex preferential orientation effects. For example, wide-angle SAED pattern of (1 1 1) plane of NaCl-type Fe_2O_3–Au superlattice shows 12 equidistant arcs for the (2 2 0) reflections of Fe_2O_3 NPs (Fig. 36d). If all Fe_2O_3 nanoparticles orient in the same

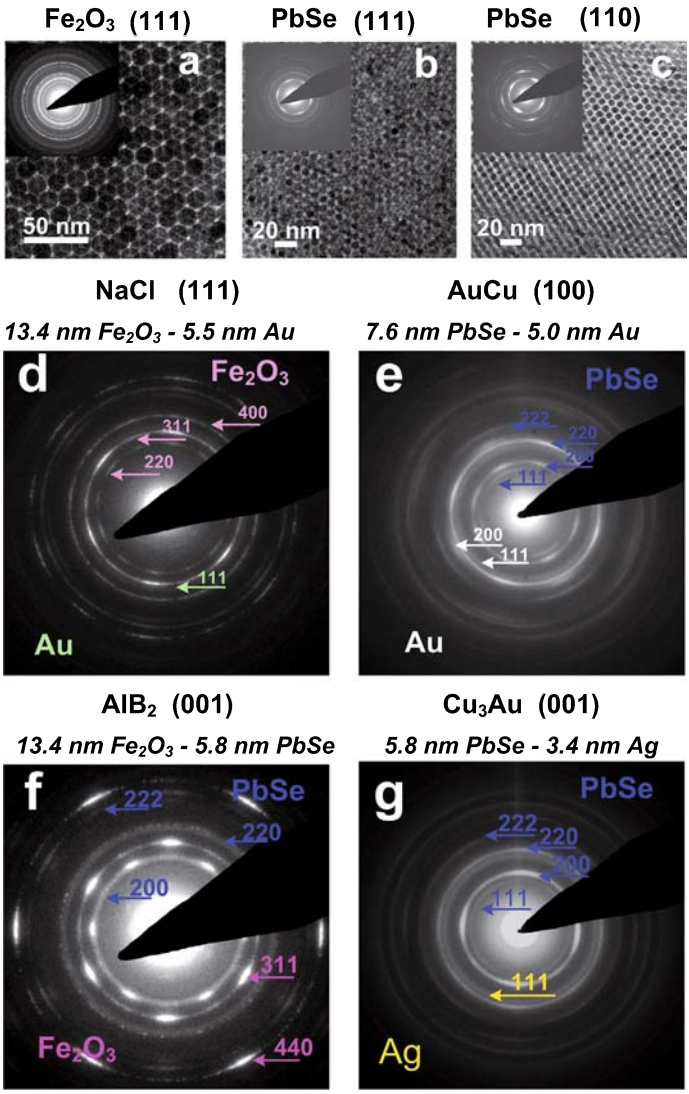

Fig. 36. TEM micrographs of **a** (111) planes of superlattices formed by 13.3 nm Fe_2O_3 nanoparticles; **b** (1 1 1) and **c** (1 1 0) planes of superlattices formed by 6.2 nm PbSe nanoparticles. Insets demonstrate the wide-angle selected area ED patterns measured from different planes. **d–g** Wide-angle selected area electron diffraction patterns measured from single-crystal domains of different BNSLs. Reproduced from [12], © 2006, with permission from the American Chemical Society

direction, we should observe four (2 2 0) diffraction spots. The 12 arcs for Fe_2O_3 (2 2 0) reflections in NaCl-type superlattice can result from 13 different orientations of Fe_2O_3 nanoparticles tilted by 60°.

Preferential orientation can be observed either for a single component or both components of binary BNSLs. Figure 36e and f shows preferential orientations for both components in PbSe–Au AuCu-type superlattice and Fe_2O_3–PbSe AlB_2-type

superlattice, respectively. Figure 36g demonstrates an example of BNSL where the larger 5.8 nm PbSe NPs show preferential orientation while smaller 3.4 nm Ag NPs are disordered. Preferential orientation should be typical for superlattices where the arrangement of nearest neighbors matches the symmetry of nanoparticle facets "locking" each nanoparticle in a specific orientation.

Different types of nanoparticle superlattices can form simultaneously on the same substrate [12]. The domains with different symmetry are usually spatially separated. However, sometimes a smooth transition between the two phases is observed. For example, Fig. 37a shows an epitaxial "super-heterostructure" formed by the (0 1 1) planes of AlB_2-type and (1 0 0) plane of *cub*-AB_{13}-type superlattices. Figure 37b demonstrates the example of the defect heterostructure between (1 1 1) plane of

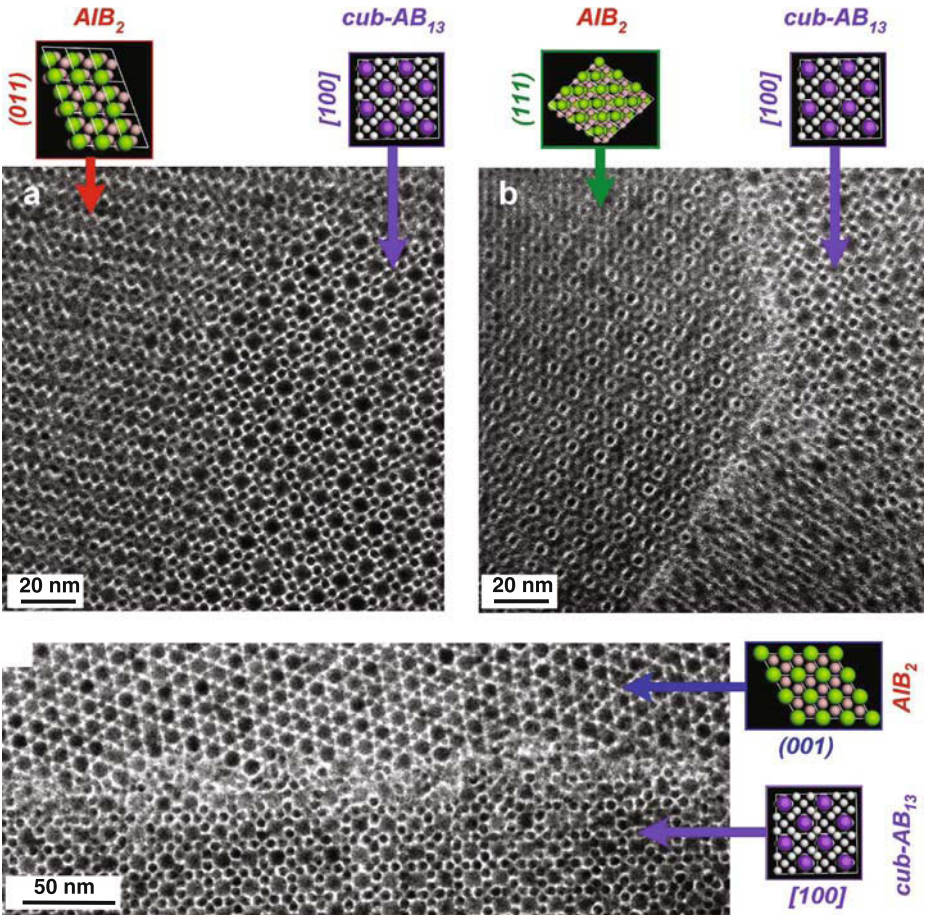

Fig. 37. TEM micrograph of **a** the epitaxial "super-heterostructure" formed by the (0 1 1) plane of AlB_2-type and (1 0 0) plane of *cub*-AB_{13}-type superlattices; **b** heterostructure formed by the (1 1 1) plane of AlB_2-type and (1 0 0) plane of *cub*-AB_{13}-type superlattices consisting of 5.8 nm PbSe and 3.0 nm Pd nanoparticles and **c** heterostructure formed by the (0 0 1) plane of AlB_2-type and (1 0 0) plane of *cub*-AB_{13}-type superlattices consisting of 7.2 nm PbSe and 4.2 nm Ag nanoparticles. Reproduced from [12],

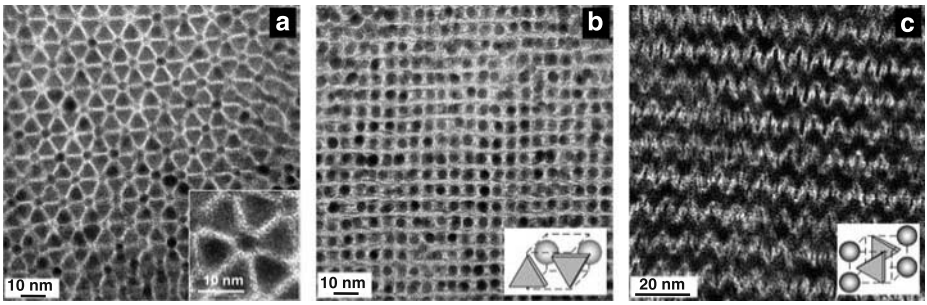

Fig. 38. TEM images of binary superlattices self-assembled (**a**, **b**) from LaF_3 triangular nanoplates (9.0 nm side) and 5.0 nm Au nanoparticles; **c** from LaF_3 triangular nanoplates and 6.2 nm PbSe nanocrystals. The insets show **a** a magnified image and **b**, **c** proposed unit cells of the corresponding superlattices. The structure shown in **a** forms on silicon nitride surface while structures shown in **b** and **c** form preferentially on amorphous carbon substrates. Reproduced from [91], © 2006, with permission from the American Chemical Society

AlB_2-type and (1 0 0) plane of *cub*-AB_{13}-type superlattice and Fig. 37c shows the example of heterostructure formed by (0 0 1) plane of AlB_2-type and (1 0 0) plane of *cub*-AB_{13}-type superlattice. This type of heterostructure can be formed as a collision of laterally growing islands of simultaneously nucleated AlB_2-type and *cub*-AB_{13}-type superlattices. Similar heterostructures were observed by Sanders in Brazilian opals [94].

In contrast to particles with amorphous or polycrystalline morphology, nanocrystals allow exploitation of the inherent crystal anisotropy to precisely engineer nanocrystal shape. The nanocrystal shape can in turn be used as a powerful tool to engineer the structure of the self-assembled BNSLs. For example, Fig. 38 shows several BNSLs self-assembled from LaF_3 triangular nanoplates and spherical Au or PbSe nanocrystals. In the LaF_3–Au system, LaF_3 nanoplates lay flat on silicon nitride membranes (Fig. 38a) and stand on edge when assembled on amorphous carbon (Fig. 38b, c) demonstrating how the choice of substrate can be used to control the structure of assembled BNSL.

It is specifically at nanoscale that the van der Waals, electrostatic, sterical repulsion, and the directional dipolar interactions can contribute to the interparticle potential with comparable weights [12]. These, together with the effects of particle substrate interactions, space-filling (entropic) factors, and specific ligand–ligand interactions determine enormous richness and diversity of structures assembled from nanoparticle building blocks. The non-equilibrium nature of evaporative self-assembly process adds additional complexity. Precise control of nanoparticle size, shape and composition allows us to engineer electronic, optical and magnetic properties of nanoparticle building blocks. Assembling these nanoscale building blocks into a wide range of BNSL systems provides powerful modular approach to the design of "metamaterials" with programmable physical and chemical properties.

5. Concluding remarks

During the last two decades semiconductor nanoparticles have developed into the new class of materials with their own sets of properties, some of them being unique

and not observable in “molecular” and “macroscopic” worlds. Recent advances in synthesis and self-assembly introduced entirely new ways of controlling the size, shape, arrangement, connectivity, and even the topology of crystalline metallic, semiconducting and oxide nanomaterials. Further progress in this direction will enable complex multi-component nanostructures to be created by design in cost-effective ways. These structures will be further used as the building blocks for different electronic, optoelectronic, magnetic and catalytic materials.

Precise assembly of nanocrystals with desired optical, electronic, and magnetic properties into single-component and binary nanoparticle superlattices provides a route to ‘metamaterials’ combining metallic, semiconducting and magnetic components into ordered superlattices; a diverse collection of these structures have been recently reported and many novel structures will follow. The modular design of multicomponent solids using nanometer scale building blocks provides access to unique combinations of properties not available in single-component bulk solids. The controllable assembly of nanoparticle into macroscopic structures with desired arrangement of the building blocks requires fundamental understanding of self-organization phenomena at the nanoscale. Significant progress has been already achieved in this area; however, little is known about collective phenomena in the nanoparticle assemblies. The presence of long-range translational ordering in nanoparticle superstructures makes them different from common amorphous and polycrystalline solids. The coupling among ordered quantum dots can lead to a splitting of the quantized carrier energy levels of single particles and result in the formation of three-dimensional minibands (Fig. 39) [95]. By changing the size of the nanocrystals, interparticle distances, barrier height, and regimentation, one can control the electronic band structure of these artificial quantum dot crystals [96]. Model calculations show that the carrier density of states, effective mass tensor and other properties of quantum dot crystals are different from those of bulk solids and quantum well superlattices [95]. Generally speaking, nanocrystal assemblies can be

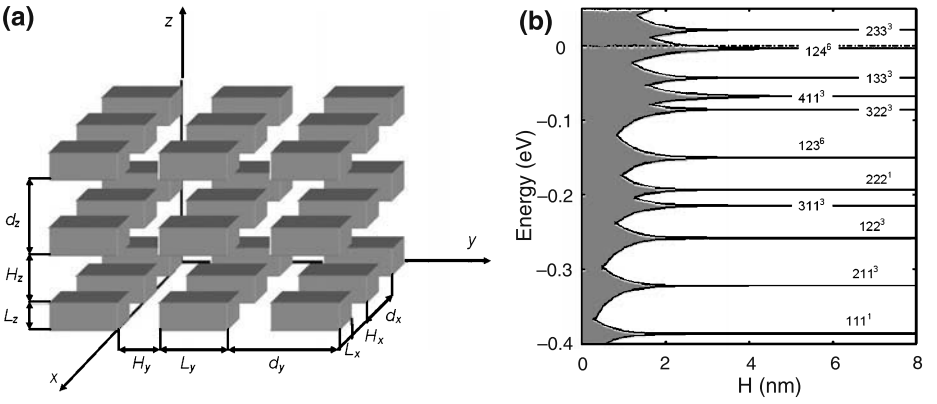

Fig. 39. **a** Schematic structure of a silicon quantum dot crystal and (**b**) its calculated electronic structure as a function of interparticle distance H. The size of the nanoparticles is $L = 6.5$ nm. At small H splitting of the quantized energy levels of single dots results in the formation of three-dimensional minibands. Reproduced from [95], © 2001, with permission from American Institute of Physics

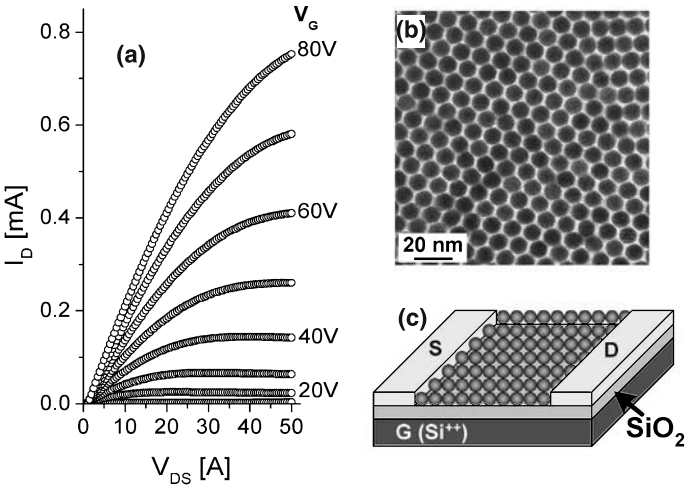

Fig. 40. **a** Electronic characteristics (drain current I_D vs. source-drain voltage V_{DS} measured for different gate voltages V_G) of a field-effect transistor with channel assembled from 9 nm PbSe nanocrystals shown in (**b**). **c** Schematics of nanocrystal-based field-effect device. Channel length 40 μm channel width 500 μm. Thickness of gate dielectric 100 nm

considered as a novel type of condensed matter, whose behavior depend both on the properties of the individual building blocks and the many body exchange interactions.

The recent studies of charge transport in superlattices of semiconductor nanocrystals demonstrated both n- and p-type transport with respectable charge carrier mobilities (>1 cm^2/V s for electrons and ~ 0.2 cm^2/V s for holes) [37] pointing to the possibility of miniband formation in properly engineered superlattices of semiconductor nanocrystals. There is a strong believe that nanocrystal assemblies can find use in inexpensive solution-processed field-effect transistors (Fig. 40), photovoltaic and thermoelectric devices [97]. At the same time, the electronic structure, phonon spectra and other characteristics of single- and multicomponent nanoparticle assemblies have never been a subject of thorough theoretical studies. Because of the absence of theoretical background, the superlattice approaches to materials design are still in the early stages of development. The generation of truly high-performance materials, requiring the optimization of many competing parameters, is still some way off. At the same time, first results represent the important steps in the rational design of nanocrystal superlattices for targeted applications.

Acknowledgements

We are deeply indebted to all our colleagues and collaborators, their names appear in the cited literature. We wish to specially thank Christopher B. Murray (University of Pennsylvania), Daan Frenkel (FOM-Institute for Atomic and Molecular Physics, Netherlands), Louis Brus, Stephen O'Brien and Irving Herman (Columbia University) for helpful discussions. E.V.S. acknowledges financial support by DOE, BES-Materials Sciences, under Contract DE-AC02-06CH11357. D.V.T. acknowledges financial support by MRSEC Program of the National Science Foundation under Award Number DMR-0213745 and FACCTS Program of the University of Chicago.

References

[1] Whitesides GM, Grzybowski B (2002) Self-assembly at all scales. Science 295: 2418–2421
[2] Yin Y, Alivisatos AP (2005) Colloidal nanocrystal synthesis and the organic–inorganic interface. Nature 437: 664–670
[3] Schmid G (ed) (2004) Nanoparticles: from theory to applications, Wiley–VCH
[4] Zeng H, Li J, Liu JP, Wang Z, Sun S (2002) Exchange-coupled nanocomposite magnets by nanoparticle self-assembly. Nature 420: 395–398
[5] Sun S, Murray CB, Weller D, Folks L, Moser A (2000) Monodisperse FePt nanoparticles and ferromagnetic nanocrystal superlattices. Science 287: 1989–1992
[6] Narayanan R, El-Sayed MA (2004) Shape-dependent catalytic activity of platinum nanoparticles in colloidal solution. Nano Letters 4: 1343–1348
[7] Alder BJ, Hoover WG, Young DA (1968) Studies in molecular dynamics. V. High-density equation of state and entropy for hard disks and spheres. Journal of Chemical Physics 49: 3688–3694
[8] Bolhuis PG, Frenkel D, Mau SC, Huse DA (1997) Entropy difference between crystal phases. Nature 388: 235–236
[9] Rudd RE, Broughton JQ (1998) Coarse-grained molecular dynamics and the atomic limit of finite elements. Physical Review B 58: 5893–5896
[10] Wang ZL (1998) Structural analysis of self-assembling nanocrystal superlattices. Advance of Materials 10: 13–30
[11] Murray CB, Kagan CR, Bawendi MG (2002) Synthesis and characterization of monodisperse nanocrystals and close-packed nanocrystal assemblies. Annual Review of Material Science 30: 545–610
[12] Shevchenko EV, Talapin DV, Murray CB, O'Brien S (2006) Structural characterization of self-assembled multifunctional binary nanoparticle superlattices. Journal of the American Chemical Society 128: 3620–3637
[13] Islam MA, Xia Y, Steigerwald ML, Yin M, Liu Z, O'Brien S, Levicky R, Herman IP (2003) Addition, suppression, and inhibition in the electrophoretic deposition of nanocrystal mixture films for CdSe nanocrystals with γ-Fe_2O_3 and Au nanocrystals. Nano Letters 3: 1603–1606
[14] Shim M, Guyot-Sionnest P (1999) Permanent dipole moment and charges in colloidal semiconductor quantum dots. Journal of Chemical Physics 111: 6955–6964
[15] Li L-S, Alivisatos AP (2003) Origin and scaling of the permanent dipole moment in CdSe nanorods. Physical Review Letters 90: 097402
[16] Rabani E, Hetenyi B, Berne DJ, Brus LE (1999) Electronic properties of CdSe nanocrystals in the absence and presence of a dielectric medium. Journal of Chemical Physics 110: 5355–5361
[17] Ohara PC, Leff DV, Heath JR, Gelbart WM (1995) Crystallization of opals from polydisperse nanoparticles. Physical Review Letters 75: 3466–3469
[18] Korgel BA, Fullam S, Connolly S, Fitzmaurice D (1998) Assembly and self-organization of silver nanocrystal superlattices: ordered "soft spheres". Journal of Physical Chemistry B 102: 8379–8388
[19] Saunders AE, Korgel BA (2004) Second virial coefficient measurements of dilute gold nanocrystal dispersions using small-angle X-ray scattering. Journal of Physical Chemistry B 108: 16732–16738
[20] Rabideau BD, Bonnecaze RT (2005) Computational predictions of stable 2D arrays of bidisperse particles. Langmuir 21: 10856–10861
[21] Berry RS, Rice SA, Ross J (2000) Physical Chemistry. Oxford University Press
[22] Chung DDL (2004) Electrical applications of carbon materials. Journal of Materials Sciences 39: 2645–2661
[23] Talapin DV, Shevchenko EV, Murray CB, Titov AV, Kral P (2007) Dipole–dipole interactions in nanoparticle superlattices. Nano Letters 7: 1213–1219
[24] Luedtke WD, Landman U (1996) Structure, dynamics, and thermodynamics of passivated gold nanocrystallites and their assemblies. Journal of Physical Chemistry 100: 13323–13329
[25] Tang ZY, Zhang ZL, Wang Y, Glotzer SC, Kotov NA (2006) Self-assembly of CdTe nanocrystals into free-floating sheets. Science 314: 274–278
[26] Klokkenburg M, Houtepen AJ, Koole R, de Folter JWJ, Erhe BH, van Faassen E, Vanmaekelbergh D (2007) Dipolar structures in colloidal dispersions of PbSe and CdSe quantum dots. Nano Letters 7: 2931–2936
[27] Tang Z, Kotov NA, Giersig M (2002) Spontaneous organization of single CdTe nanoparticles into luminescent nanowires. Science 297: 237–240
[28] Pacholski C, Kornowski A, Weller H (2002) Self-assembly of ZnO: from nanodots to nanorods. Angewandte Chemie International Edition 41: 1188–1191

[29] Cho K-S, Talapin DV, Gaschler W, Murray CB (2005) Designing PbSe nanowires and nanorings through oriented attachment of nanoparticles. Journal of the American Chemical Society 127: 7140–7147
[30] Shanbhag S, Kotov NA (2006) On the origin of a permanent dipole moment in nanocrystals with a cubic crystal lattice: effects of truncation, stabilizers, and medium for CdS tetrahedral homologues. Journal of Physical Chemistry B 110: 12211–12217
[31] Cui Y, Zhong Z, Wang D, Wang WU, Lieber CM (2003) High performance silicon nanowire field effect transistors. Nano Letters 3: 149–152
[32] Patolsky F, Zheng G, Hayden O, Lakadamyali M, Zhuang X, Lieber CM (2004) Electrical detection of single viruses. Proceedings of the National Academy of Sciences of the United States of America 101: 14017–14022
[33] Hahm J-I, Lieber CM (2004) Direct ultrasensitive electrical detection of DNA and DNA sequence variations using nanowire nanosensors. Nano Letters 4: 51–54
[34] Huynh WU, Dittmer JJ, Alivisatos AP (2002) Hybrid nanorod–polymer solar cells. Science 295: 2425–2427
[35] Hicks LD, Dresselhaus MS (1993) Thermoelectric figure of merit of a one-dimensional conductor. Physical Review B 47: 16631–16634
[36] Lin YM, Dresselhaus MS (2003) Thermoelectric properties of superlattice nanowires. Physical Review B 68: 075304
[37] Talapin DV, Murray CB (2005) PbSe nanocrystal solids for n- and p-channel thin film field-effect transistors. Science 310: 86–89
[38] Rabani E, Reichman PL, Brus LE (2003) Drying-mediated self-assembly of nanoparticles. Nature 426: 271–274
[39] Tanaka H (2000) Viscoelastic phase separation. Journal of Physics: Condensed Matter 12: R207–R264
[40] Ohara PC, Heath JR, Gelbart WM (1997) Self-assembly of submicrometer rings of particles from solutions of nanoparticles. Angewandte Chemie International Edition 15: 1078–1080
[41] Heath JR, Knobler CM, Leff DV (1997) Pressure/temperature phase diagrams and superlattices of organically functionalized metal nanocrystal monolayers: the influence of particle size, size distribution, and surface passivant. Journal of Physical Chemistry B 101: 189–197
[42] Dabbousi BO, Murray CB, Rubner MF, Bawendi MG (1994) Langmuir–Blodgett manipulation of size-selected CdSe nanocrystallites. Chemistry of Materials 6: 216–219
[43] Ge G, Brus L (2000) Evidence for spinodal phase separation in two-dimensional nanocrystal self-assembly. Journal of Physical Chemistry B 104: 9573–9575
[44] Maillard M, Motte A, Ngo AT, Pileni MP (2000) Rings and hexagons made of nanocrystals: a Marangoni effect. Journal of Physical Chemistry B 104: 11871–11877
[45] Gelbart WM, Sear RP, Heath JR, Chaney S (1999) Array formation in nano-colloids: theory and experiment in 2D. Faraday Discusions 112: 299–307
[46] Ohara PC, Gelbart WM (1998) Interplay between hole instability and nanoparticle array formation in ultrathin liquid films. Langmuir 14: 3418–3424
[47] Ondarcuhu T, Millan-Rodriguez J, Mancini HL, Garcimartin A, Perez-Garcia C (1993) Benard–Marangoni convective patterns in small cylindrical layers. Physical Review E 48: 1051–1057
[48] Sukhanova A, Baranov AV, Perova TS, Cohen JHM, Nabiev (2006) Controlled self-assembly of nanocrystals into polycrystalline fluorescent dendrites with energy-transfer properties. Angewandte Chemie International Edition 45: 2048–2052
[49] Norris DJ, Arlinghaus EG, Meng L, Heiny R, Scriven LE (2004) Opaline photonic crystals: how does self-assembly work? Advanced Materials 16: 1393–1399
[50] Hynninen A-P, Dijkstra M (2005) Phase diagram of dipolar hard and soft spheres: manipulation of colloidal crystal structures by an external field. Physical Review Letters 94: 138303–138306
[51] Murray CB, Kagan CR, Bawendi MG (1995) Self-organization of CdSe nanocrystallites into three-dimensional quantum dot superlattices. Science 270: 1335–1338
[52] Talapin DV, Shevchenko EV, Kornowski A, Gaponik N, Haase M, Rogach AL, Weller H (2001) A new approach to crystallization of CdSe nanoparticles into ordered three-dimensional superlattices. Advanced Materials 13: 1868–1871
[53] Shevchenko E, Talapin D, Kornowski A, Wiekhorst F, Koetzler J, Haase M, Rogach A, Weller H (2002) Colloidal crystals of monodisperse FePt nanoparticles grown by a three-layer technique of controlled oversaturation. Advanced Materials 14: 287–290
[54] Shevchenko EV, Talapin DV, Rogach, AL, Kornowski A, Haase M, Weller H (2002) Colloidal synthesis and self-assembly of $CoPt_3$ nanocrystals. Journal of the American Chemical Society 124: 11480–11485

[55] Nagel M, Hickey SG, Frömsdorf A, Kornowski A, Weller H (2007) Synthesis of monodisperse PbS nanoparticles and their assembly into highly ordered 3D colloidal crystals. Zeitschrift für Physikalische Chemie 221: 427–437
[56] Borchert H, Shevchenko EV, Robert A, Mekis I, Kornowski A, Grubel G, Weller H (2005) Determination of nanocrystal sizes: a comparison of TEM, SAXS, and XRD studies of highly monodisperse $CoPt_3$ particles. Langmuir 21: 1931–1936
[57] Blanto SA, Leheny RL, Hines MA, Guyot-Sionnest P (1997) Dielectric dispersion measurements of CdSe nanocrystal colloids: observation of a permanent dipole moment. Physical Review Letters 79: 865–868
[58] Pusey PN (1991) Colloidal suspensions. In: Liquids, freezing and glass transition Hansen JP, Levesque D, Zinn-Justin J (eds.), North-Holland, Amsterdam, pp. 765–942
[59] Auer S, Frenkel D (2001) Suppression of crystal nucleation in polydisperse colloids due to increase of the surface free energy. Nature 413: 711–713
[60] Pronk S, Frenkel D (2001) Point defects in hard-sphere crystals. Journal of Physical Chemistry B 105: 6722–6727
[61] Pronk S, Frenkel D (2004) Large effect of polydispersity on defect concentrations in colloidal crystals. Journal of Chemical Physics 120: 6764–6772
[62] Manna L, Scher EC, Alivisatos AP (2000) Synthesis of soluble and processable rod-, arrow-, teardrop-, and tetrapod-shaped CdSe nanocrystals. Journal of the American Chemical Society 122: 12700–12706
[63] Peng X (2002) Green chemical approaches toward high quality semiconductor nanocrystals. Chemistry-A European Journal 8: 335–340
[64] Peng X, Manna L, Yang W, Wickham J, Scher E, Kadavanich A, Alivisatos AP (2000) Shape control of CdSe nanocrystals. Nature 404: 59–61
[65] Li L-S, Hu J, Yang W, Alivisatos AP (2001) Band gap variation of size- and shape-controlled colloidal CdSe quantum rods. Nano Letters 1: 349–351
[66] Hu J, Li L-S, Yang W, Manna L, Wang L-W, Alivisatos AP (2001) Linearly polarized emission from colloidal semiconductor quantum rods. Science 292: 2060–2063
[67] Frenkel D, Lekkerkerker HNW, Stroobants A (1988) Thermodynamic stability of a smectic phase in a system of hard rods. Nature 332: 822–823
[68] Schilling T, Frenkel D (2004) Self-poisoning of crystal nuclei in hard-rod liquids. Physical Review Letters 92: 085505–085508
[69] McGrother SC, Williamson DC, Jackson G (1996) A re-examination of the phase diagram of hard spherocylinders. Journal of Chemical Physics 104: 6755–6759
[70] Frenkel D (1988) Structure of hard-core models for liquid crystals. Journal of Physical Chemistry 92: 3280–3284
[71] Schilling T, Frenkel D (2004) Self-poisoning of crystal nuclei in hard-rod liquids. Journal of Physics: Condensed Matter 16: S2029–S2036
[72] McGrother C, Gil-Villegas A, Jackson G (1996) The liquid-crystalline phase behavior of hard spherocylinders with terminal point dipoles. Journal of Physics: Condensed Mater 8: 9649–9655
[73] Li L-S, Walda J, Manna L, Alivisatos AP (2002) Semiconductor nanorod liquid crystals. Nano Letters 2: 557–560
[74] Talapin DV, Shevchenko EV, Murray CB, Kornowski A, Forster S, Weller H (2004) CdSe and CdSe/CdS nanorod solids. Journal of the American Chemical Society 126: 12984–12988
[75] Carbone L, Nobile C, De Giorgi M, Sala FD, Morello G, Pompa P, Hytch M, Snoeck E, Fiore A, Franchini IR, Nadasan M, Silvestre AF, Chiodo L, Kudera S, Cingolani R, Krahne R, Manna, L (2007) Synthesis and micrometer-scale assembly of colloidal CdSe/CdS nanorods prepared by a seeded growth approach. Nano Letters 7: 2942–2950
[76] Phillips PJ (1994) Spherulitic crystallization in macromolecules. In: Handbook of crystal growth (Hurtle DTJ, ed.) North-Holland: Amsterdam, pp. 1168–1215
[77] Singfield KL, Hobbs JK, Keller A (1998) Correlation between main chain chirality and crystal twist direction in polymer spherulites. Journal of Crystal Growth 183: 683–689
[78] Talapin DV, Nelson JH, Shevchenko EV, Aloni S, Sadtler B, Alivisatos AP (2007) Seeded growth of highly luminescent CdSe/CdS nanoheterostructures with rod and tetrapod morphologies. Nano Letters 7: 2951–2959
[79] Talapin DV, Koeppe R, Gotzinger S, Kornowski A, Lupton JM, Rogach AL, Benson O, Feldmann J, Weller H (2003) Highly emissive colloidal CdSe/CdS heterostructures of mixed dimensionality. Nano Letters 3: 1677–1681
[80] Ryan KM, Mastroianni A, Stancil KA, Liu H, Alivisatos AP (2006) Electric-field-assisted assembly of perpendicularly oriented nanorod superlattices. Nano Letters 6: 1479–1482

[81] Manna L, Milliron DJ, Meisel A, Scher EC, Alivisatos AP (2003) Controlled growth of tetrapod-branched inorganic nanocrystals. Nature Materials 2: 382–385
[82] Blaak R, Mulder BM, Frenkel D (2004) Cubatic phase for tetrapods. Journal of Chemical Physics 120: 5486–5492
[83] Eldridge MD, Madden PA, Frenkel D (1993) The stability of the AB13 crystal in a binary hard sphere system. Molecular Physics 79: 105–120
[84] Trizac E, Eldridge MD, Madden PA (1997) Stability of the AB crystal for asymmetric binary hard sphere mixtures. Molecular Physics 90: 675–678
[85] Cottin X, Monson PA (1995) Substitutionally ordered solid solutions of hard spheres. Journal of Chemical Physics 102: 3354–3361
[86] Murray MJ, Sanders JV (1980) Close-packed structures of spheres of two different sizes. II. The packing densities of likely arrangements. Philosophical Magazine A 42: 721–740
[87] Sanders JV, Murray MJ (1978) Ordered arrangements of spheres of two different sizes in opal. Nature 275: 201–203
[88] Hachisu S, Yoshimura S (1980) Optical demonstration of crystalline superstructures in binary mixtures of latex globules. Nature 283: 188–189
[89] Bartlett P, Ottewill RH, Pusey PN (1992) Superlattice formation in binary mixtures of hard-sphere colloids. Physical Review Letters 68: 3801–3804
[90] Eldridge MD, Madden PA, Frenkel D (1993) Entropy-driven formation of a superlattice in a hard-sphere binary mixture. Nature 365: 35–37
[91] Shevchenko EV, Talapin DV, Kotov NA, O'Brien S, Murray CB (2006) Structural diversity in binary nanoparticle superlattices. Nature 439: 55–59
[92] Leunissen ME, Christova CG, Hynninen A-P, Royall CP, Campbell AI, Imhof A, Dijkstra M, van Roij R, van Blaaderen A (2005) Ionic colloidal crystals of oppositely charged particles. Nature 437: 235–240
[93] O'Brien RW, White LR (1978) Electrophoretic mobility of a spherical colloidal particle. Journal of the Chemical Society-Faraday Transactions II 74: 1607–1626
[94] Sanders JV (1980) Close-packed structures of spheres of two different sizes I. Observations on natural opal. Philosophical Magazine A 42: 705–720
[95] Lazarenkova OL, Balandin AA (2001) Miniband formation in a quantum dot crystal. Journal of Applied Physics 89: 5509–5513
[96] Jiang C-W, Green MA (2006) Silicon quantum dot superlattices: Modeling of energy bands, densities of states, and mobilities for silicon tandem solar cell applications. Journal of Applied Physics 99: 114902
[97] Urban JJ, Talapin DV, Shevchenko EV, Kagan CR, Murray CB (2007) Synergism in binary nanocrystal superlattices leads to enhanced p-type conductivity in self-assembled PbTe/Ag_2Te thin films. Nature Materials 6: 115–121